

A 2-D Velocity Structure for a Cross-Cascades Profile
Using Earthquake Sources

by

Andreas P. Schultz

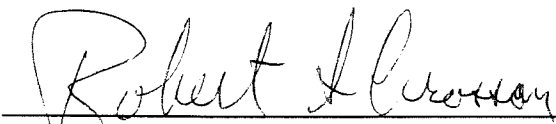
A thesis submitted in partial fulfillment
of the requirements for the degree of

Master of Science

University of Washington

1993

Approved by



(Chairperson of the Supervisory Committee)

Program Authorized
to Offer Degree

Geophysics Program

Date

June 8, 1993

Master's Thesis

In presenting this thesis in partial fulfillment of the requirement for a Master's degree at the University of Washington, I agree that the library shall make its copies freely available for inspection. I further agree that extensive copying of this thesis is allowable only for scholarly purposes, consistent with "fair use" as prescribed in the U.S. Copyright Law. Any other reproduction for any purposes or by any means shall not be allowed without my written permission.

Signature _____

Date _____

University of Washington

Abstract

**A 2-D Velocity Structure for a Cross-Cascades
Profile Using Earthquake Sources**

by

Andreas P. Schultz

Chairperson of Supervisory Committee: Professor Robert S. Crosson
Geophysics Program

A 2-dimensional velocity model extending to depths of about 50 km was created for a profile extending from Bremerton to Walla Walla in Washington state. The method employed existing network stations and earthquake sources for a refraction/wide-angle reflection study. The final model consisted of a five layer crust overlying the upper mantle. Crustal velocities directly under the Cascades along the profile were slow relative to adjacent areas near the top of the model, but this feature disappeared below a depth of 25 km. Results from reflectivity synthetic modeling suggest that the Moho represents a transition zone of some thickness rather than a discrete boundary. The continental Moho was found to have a dip of 2.7° to the west in eastern Washington and 4.4° to the east beneath the Puget Sound. Maximum crustal thicknesses ranged from 35.5 km under the Puget Sound and 34 km near Walla Walla in eastern Washington to 47 km under the high Cascades.

Table of Contents

	page
List of Figures	ii
List of Tables	iv
Chapter I -- Introduction	1
Project Goals	2
Geological Summary	3
Method of Investigation	4
Principal Results	5
Chapter II -- Data and Station Locations	7
Chapter III -- Summary of Ray Tracing and Inversion	15
Ray Tracing and Inversion	16
Chapter IV -- Travel Time Modeling	18
The Starting Model	18
The Final Model	20
Chapter V -- Discussion of Travel Time Modeling	24
Comparison with Gravity	30
Resolution and Variance	32
Chapter VI -- Reflectivity Synthetics.....	39
Discussion	41
Chapter VII -- Conclusions	45
Bibliography	47
Appendix I : Stations used.....	50
Appendix II : Earthquakes used	51
Appendix III : Station movement	52
Appendix IV : 1-D starting models	53
Appendix V : Resolution and standard errors	54

List of Figures

	page
Figure 1 -- Base Map of Washington State and Study Area	3
Figure 2 -- Source-Receiver Geometry: Case 1	7
Figure 3 -- Source-Receiver Geometry: Case 2	8
Figure 4 -- Cross-section of Worst Station Movement	10
Figure 5 -- Reduced Record Section for Typical Event	12
Figure 6 -- Typical Picks from Real Data	13
Figure 7 -- Proximity of Epicenters to Profile	14
Figure 8 -- Vertical Distribution of Sources	14
Figure 9 -- 2-D Starting Velocity Model	19
Figure 10 -- Quantitative Cross-Section of Final Velocity Model	21
Figure 11 -- Density Plot of Final Velocity Model	22
Figure 12 -- Ray Tracing and Reduced Travel Time (#1 and #2)	26
Figure 13 -- Ray Tracing and Reduced Travel Time (#10 and #21)	27
Figure 14 -- Ray Tracing w/ Flat Model Interface	29
Figure 15a - Travel Time Residuals for Starting Model	34
Figure 15b - Travel Time Residuals for Final Model	34
Figure 16 -- Resolution for Final Model	36
Figure 17 -- Ray Coverage in Final Model	38

	page
Figure 18 -- 1-D Starting Velocity Model for Synthetics	40
Figure 19 -- Comparison of Real and Synthetic Waveforms	46
Figure 20 -- Comparison of Real Data and Two Synthetics	43

List of Tables

	page
Appendix I, Table A1 -- Stations and Their Geographic Locations.....	50
Appendix II, Table A2 -- Earthquake Locations and X-Distances.....	51
Appendix III, Table A3 -- Actual Station Movement	52
Appendix IV, Table A4 -- 1-Dimensional Starting Models.....	53
Appendix V, Table A5 -- Resolution and Std Error for Velocity Nodes.....	54

ACKNOWLEDGEMENTS

I wish to express my sincere appreciation to the members of my Masters committee, Dr. Bob Crosson, Dr. Ken Creager, and Dr. Steve Malone, for reviewing the document and making many helpful suggestions. I would also like to thank Ken Creager and Bob Crosson for the many long discussions and the endless good suggestions they made en route to my completing this thesis. I would like to thank my office mate, Shawn Dewberry, for answering all the questions that tended to pop up on a daily basis, and I would especially like to thank him for helping me master the art of Frame-Maker. Along those same lines, I would like to express my appreciation to Ken Creager for helping me understand MATLAB and to John Winchester for the same with Mathematica. Resident experts are the best source of information. Finally, I would like to thank the weather forecasters in the greater Seattle area for scheduling a plethora of bad weather during the time I wrote this document -- their timing was impeccable.

Chapter I -- INTRODUCTION

The structure of the Earth's crust and upper mantle is one of the foremost objectives in geophysics. Seismological analysis contributes greatly to this objective, and deep seismic refraction/reflection methods have been applied extensively in modern seismology. Trends in shallow seismicity reveal faults and other possible hazards to human dwellings and other engineered structures. The clustering of events in areas of known volcanism can be used to infer the location and size of an existing magma chamber [Moran, 1992], which in turn can give some indication about a volcano's ability or likelihood to erupt. Techniques of interpretation of seismic refraction/reflection data have been refined extensively in recent years, and now inversion methods are often applied to such data [Zelt and Smith, 1992, Gridley, 1993].

While most seismic refraction/reflection experiments are conducted using active (explosive or vibrator) sources, the use of earthquakes as sources can be made in unusual circumstances where the density, spread, and duration of network recording stations is sufficient. The advantages provided by using earthquake sources include a vertical distribution of sources that assures sufficient angular ray coverage at depth and a large dataset from which to select sources. Disadvantages and limitations are encountered because source locations are not precisely known, and sources as well as receivers must be approximately located along a linear profile line.

This study focuses on developing a 2-D compressional wave velocity model across the Cascade Range of Washington state. Since little is known about the change of seismic velocity across the Cascades, this study contributes essential velocity structure information that illuminates the transition from the Columbia Plateau to the Puget Sound.

Additionally, this study determines the depth to the Moho interface and other significant subsurface reflectors.

There is much speculation regarding the existence of a mountain root underlying the Cascade Range. Johnson and Couch (1970) did not find evidence for a significant root for the Cascades as a whole, but their derived crustal thicknesses of 30 km did not match the predicted Moho depth based on observed Bouguer Gravity anomalies either. The Bouguer Gravity Anomaly map of Washington state [Bonini *et al.*, 1974] suggests considerable Moho depression under the Cascades if a conventional Airy model of isostatic compensation is assumed. By using PmP (Moho reflections) as well as Pn (headwaves) and other refracted arrivals, this study reaches firmer conclusions regarding the existence of the root needed for isostatic compensation of the Cascades.

Project Goals

The goal of this study is to construct a two-dimensional velocity model for a profile extending from Bremerton in the Puget Sound area to Walla Walla in eastern Washington (Figure 1) by using a refraction/wide-angle reflection approach. In the process I hope to address such issues as the depth to the various reflecting interfaces, especially the Moho, and the general shape of these interfaces. What separates this study from other studies is the use of earthquake sources along the profile rather than the more traditional explosive sources. This removes some limitations of surface-surface data because my data set includes events at considerable depth ($z > 50km$). With this approach, angular ray coverage at depth is increased, hopefully increasing the resolution of the final model at Moho depths [White, 1989]. Additional constraints are imposed by wide-angle reflections (PmP) off the Moho and by headwave (Pn) arrivals.

A 2-D Velocity Structure for a Cross-Cascades Profile
Using Earthquake Sources

by

Andreas P. Schultz

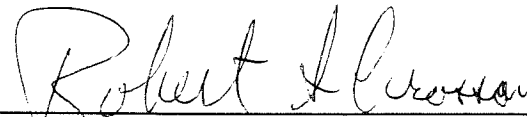
A thesis submitted in partial fulfillment
of the requirements for the degree of

Master of Science

University of Washington

1993

Approved by



(Chairperson of the Supervisory Committee)

Program Authorized

to Offer Degree Geophysics Program

Date June 8, 1993

Master's Thesis

In presenting this thesis in partial fulfillment of the requirement for a Master's degree at the University of Washington, I agree that the library shall make its copies freely available for inspection. I further agree that extensive copying of this thesis is allowable only for scholarly purposes, consistent with "fair use" as prescribed in the U.S. Copyright Law. Any other reproduction for any purposes or by any means shall not be allowed without my written permission.

Signature _____

Date _____

University of Washington

Abstract

**A 2-D Velocity Structure for a Cross-Cascades
Profile Using Earthquake Sources**

by

Andreas P. Schultz

Chairperson of Supervisory Committee: Professor Robert S. Crosson
Geophysics Program

A 2-dimensional velocity model extending to depths of about 50 km was created for a profile extending from Bremerton to Walla Walla in Washington state. The method employed existing network stations and earthquake sources for a refraction/wide-angle reflection study. The final model consisted of a five layer crust overlying the upper mantle. Crustal velocities directly under the Cascades along the profile were slow relative to adjacent areas near the top of the model, but this feature disappeared below a depth of 25 km. Results from reflectivity synthetic modeling suggest that the Moho represents a transition zone of some thickness rather than a discrete boundary. The continental Moho was found to have a dip of 2.7° to the west in eastern Washington and 4.4° to the east beneath the Puget Sound. Maximum crustal thicknesses ranged from 35.5 km under the Puget Sound and 34 km near Walla Walla in eastern Washington to 47 km under the high Cascades.

Table of Contents

	page
List of Figures	ii
List of Tables	iv
Chapter I -- Introduction	1
Project Goals	2
Geological Summary	3
Method of Investigation	4
Principal Results	5
Chapter II -- Data and Station Locations	7
Chapter III -- Summary of Ray Tracing and Inversion	15
Ray Tracing and Inversion	16
Chapter IV -- Travel Time Modeling	18
The Starting Model	18
The Final Model	20
Chapter V -- Discussion of Travel Time Modeling	24
Comparison with Gravity	30
Resolution and Variance	32
Chapter VI -- Reflectivity Synthetics.....	39
Discussion	41
Chapter VII -- Conclusions	45
Bibliography	47
Appendix I : Stations used.....	50
Appendix II : Earthquakes used	51
Appendix III : Station movement	52

List of Figures

	page
Figure 1 -- Base Map of Washington State and Study Area	3
Figure 2 -- Source-Receiver Geometry: Case 1	7
Figure 3 -- Source-Receiver Geometry: Case 2	8
Figure 4 -- Cross-section of Worst Station Movement	10
Figure 5 -- Reduced Record Section for Typical Event	12
Figure 6 -- Typical Picks from Real Data	13
Figure 7 -- Proximity of Epicenters to Profile	14
Figure 8 -- Vertical Distribution of Sources	14
Figure 9 -- 2-D Starting Velocity Model	19
Figure 10 -- Quantitative Cross-Section of Final Velocity Model	21
Figure 11 -- Density Plot of Final Velocity Model	22
Figure 12 -- Ray Tracing and Reduced Travel Time (#1 and #2)	26
Figure 13 -- Ray Tracing and Reduced Travel Time (#10 and #21)	27
Figure 14 -- Ray Tracing w/ Flat Model Interface	29
Figure 15a - Travel Time Residuals for Starting Model	34

page

Figure 18 -- 1-D Starting Velocity Model for Synthetics40

Figure 19 -- Comparison of Real and Synthetic Waveforms 46

Figure 20 -- Comparison of Real Data and Two Synthetics 43

List of Tables

	page
Appendix I, Table A1 -- Stations and Their Geographic Locations.....	50
Appendix II, Table A2 -- Earthquake Locations and X-Distances.....	51
Appendix III, Table A3 -- Actual Station Movement	52
Appendix IV, Table A4 -- 1-Dimensional Starting Models.....	53
Appendix V, Table A5 -- Resolution and Std Error for Velocity Nodes.....	54

ACKNOWLEDGEMENTS

I wish to express my sincere appreciation to the members of my Masters committee, Dr. Bob Crosson, Dr. Ken Creager, and Dr. Steve Malone, for reviewing the document and making many helpful suggestions. I would also like to thank Ken Creager and Bob Crosson for the many long discussions and the endless good suggestions they made en route to my completing this thesis. I would like to thank my office mate, Shawn Dewberry, for answering all the questions that tended to pop up on a daily basis, and I would especially like to thank him for helping me master the art of Frame-Maker. Along those same lines, I would like to express my appreciation to Ken Creager for helping me understand MATLAB and to John Winchester for the same with Mathematica. Resident experts are the best source of information. Finally, I would like to thank the weather forecasters in the greater Seattle area for scheduling a plethora of bad weather during the time I wrote this document -- their timing was impeccable.

Chapter I -- INTRODUCTION

The structure of the Earth's crust and upper mantle is one of the foremost objectives in geophysics. Seismological analysis contributes greatly to this objective, and deep seismic refraction/reflection methods have been applied extensively in modern seismology. Trends in shallow seismicity reveal faults and other possible hazards to human dwellings and other engineered structures. The clustering of events in areas of known volcanism can be used to infer the location and size of an existing magma chamber [Moran, 1992], which in turn can give some indication about a volcano's ability or likelihood to erupt. Techniques of interpretation of seismic refraction/reflection data have been refined extensively in recent years, and now inversion methods are often applied to such data [Zelt and Smith, 1992, Gridley, 1993].

While most seismic refraction/reflection experiments are conducted using active (explosive or vibrator) sources, the use of earthquakes as sources can be made in unusual circumstances where the density, spread, and duration of network recording stations is sufficient. The advantages provided by using earthquake sources include a vertical distribution of sources that assures sufficient angular ray coverage at depth and a large dataset from which to select sources. Disadvantages and limitations are encountered because source locations are not precisely known, and sources as well as receivers must be approximately located along a linear profile line.

This study focuses on developing a 2-D compressional wave velocity model

Additionally, this study determines the depth to the Moho interface and other significant subsurface reflectors.

There is much speculation regarding the existence of a mountain root underlying the Cascade Range. Johnson and Couch (1970) did not find evidence for a significant root for the Cascades as a whole, but their derived crustal thicknesses of 30 km did not match the predicted Moho depth based on observed Bouguer Gravity anomalies either. The Bouguer Gravity Anomaly map of Washington state [Bonini *et al.*, 1974] suggests considerable Moho depression under the Cascades if a conventional Airy model of isostatic compensation is assumed. By using PmP (Moho reflections) as well as Pn (head-waves) and other refracted arrivals, this study reaches firmer conclusions regarding the existence of the root needed for isostatic compensation of the Cascades.

Project Goals

The goal of this study is to construct a two-dimensional velocity model for a profile extending from Bremerton in the Puget Sound area to Walla Walla in eastern Washington (Figure 1) by using a refraction/wide-angle reflection approach. In the process I hope to address such issues as the depth to the various reflecting interfaces, especially the Moho, and the general shape of these interfaces. What separates this study from other studies is the use of earthquake sources along the profile rather than the more traditional explosive sources. This removes some limitations of surface-surface data because my data set includes events at considerable depth ($z > 50\text{km}$). With this approach, angular

Reflectivity synthetics could provide insight into the sharpness of the Moho interface. This should provide an effective double-check on whether the Moho represents a sharp discontinuity or a transition zone of finite thickness.

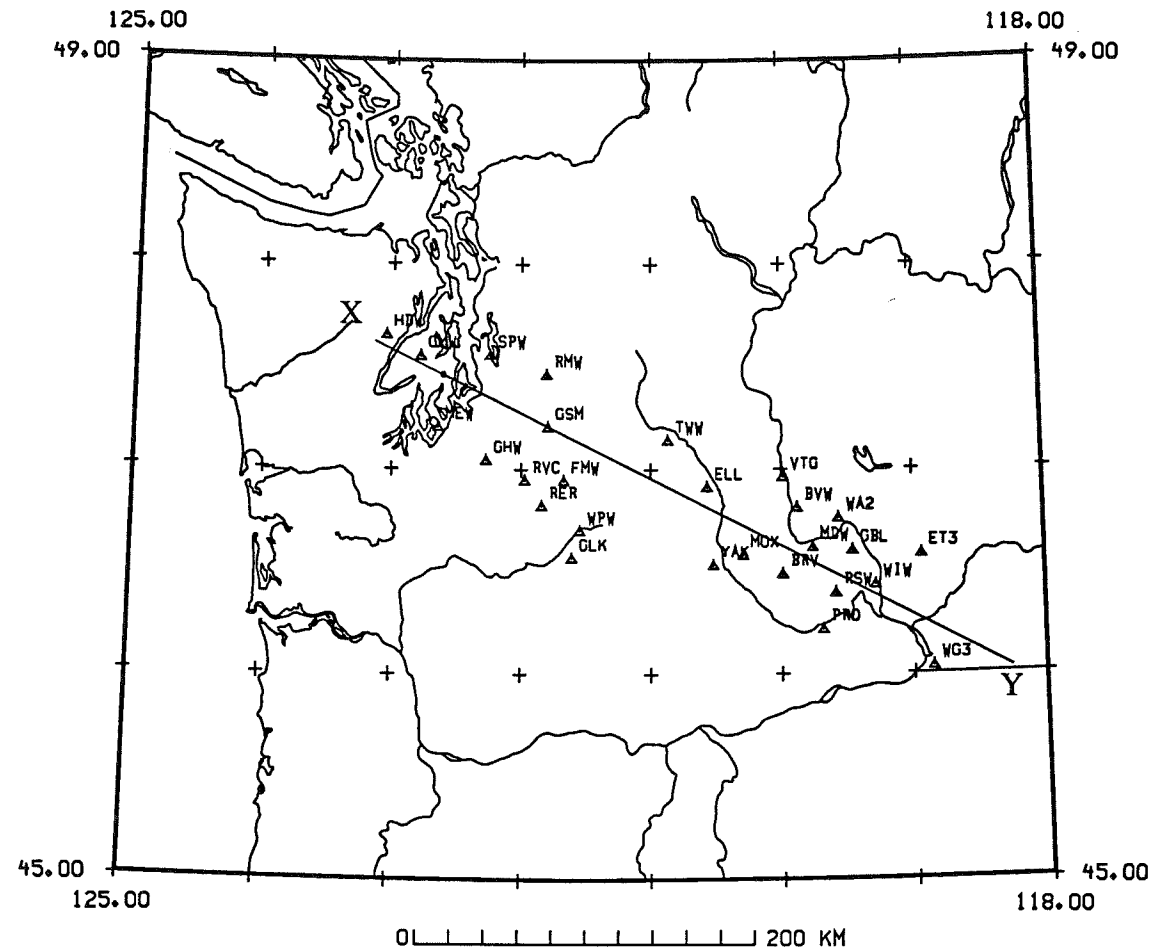


FIGURE 1. Base map of Washington state showing the seismic stations used in the study and the azimuth of the profile. Stations can be found in Appendix I, Table A1.

largely determined by the type of rock encountered by the rays, thus a summary of the geology along the profile is helpful in interpreting the final velocities.

The surface geology in the Puget Sound basin consists mainly of Quaternary continental glacial till. Basement rock consists mainly of Tertiary volcanics [Cowan and Potter, 1986]. The andesite near the southeastern edge of the Puget Sound basin extends into the Cascades where, along with rhyolite and flow breccias, it becomes one of the main constituents of the Cascade surface geology in the vicinity of the profile [Walsh *et al.*, 1987]. Geology at depth probably includes intrusive volcanics, pyroclastic flows, and andesite flows interbedded with sandstone, shale and chert.

The Columbia Plateau consists of a thin surface layer of unconsolidated sediments overlying the Columbia River Basalt group, which composes nearly the entire plateau and consists of volcanics ranging in age from Eocene to Pliocene [McKee, 1972]. Subsurface geology includes formations of interbedded shale, siltstone, sandstone, and gneiss [Gresens, 1983]. The exact extent of these formations into parts of the Plateau is unknown, but it is likely that the gneiss may represent the crystalline basement under the Columbia Plateau, as well as under the Cascades and Puget Sound.

Method of Investigation

The study area and the available dataset lends itself to the utilization of seismic refraction/wide-angle reflection methods. It was possible to obtain refracted P, Pn, and PmP arrivals from the data. It was also possible to reverse the profile completely to add

The travel times obtained from the selected dataset of earthquakes and network stations were modeled using ray theory in a 2-D velocity model. The forward ray tracing and the subsequent least-squares inversion was performed using computer code written by Colin Zelt (Zelt and Smith, 1992). The 2-D ray tracing algorithm, which will be discussed in more detail later, inverted seismic travel times and solved for 2-D velocity and interface structure simultaneously.

The final velocity model was checked by comparing a synthetic seismogram calculated with the reflectivity method with a real short-period seismogram from one of the network stations. This method tested whether the impedance contrast and the sharpness of the Moho determined from the ray tracing and inversion were reasonable. The reflectivity synthetics were calculated using a P-SV reflectivity code written by Subhashis Mallick. The practical aspects of reflectivity modeling are discussed by Mallick and Frazer (1987), but a short summary will be given later.

Principal Results

A two-dimensional velocity model extending to depths of about 50 km was developed for the profile. A total of 25 earthquakes and 27 stations were used providing 376 observed raypaths through the model. The final model traced 362 raypaths or 96.3% of the possible rays with an overall RMS = .193 seconds.

The final model consisted of a five layer crust overlying the mantle. Crustal velocities directly under the Cascades Range were slow relative to adjacent regions. This sug-

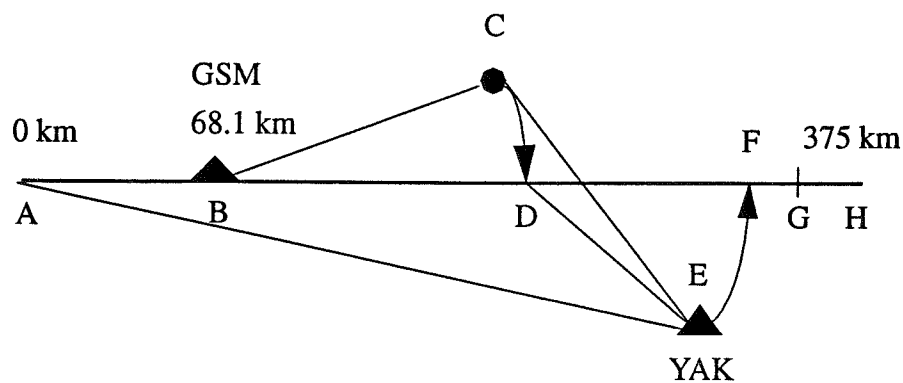
“root”. The maximum crustal thickness under the high Cascades was 47 km, shallowing to 34 km in eastern Washington and to 35.5 km under the Puget Sound.

Reflectivity modeling efforts in eastern Washington were largely inconclusive because near-surface geology beneath the network station resulted in a waveform with nearly indistinguishable phases. The reflectivity synthetics suggest, however, that the Moho beneath eastern Washington does not represent a sharp boundary but may be a zone of strong vertical velocity gradient.

Chapter II -- DATA AND STATION LOCATIONS

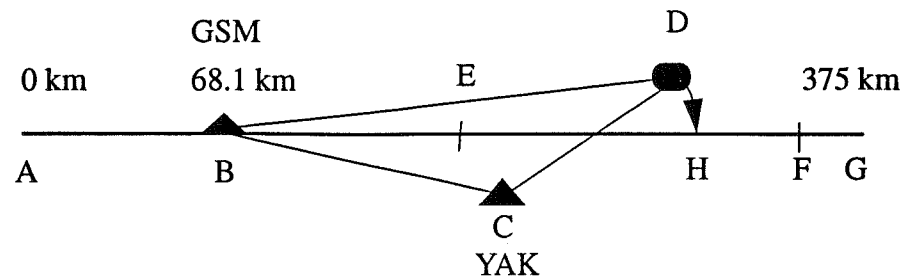
Traditional seismic refraction profiles consist of linear arrays of receivers (sources) at dense spacing appropriate to the resolution needed for the study. Sources are generally chemical explosions or mechanical vibrators. The current study utilizes an existing distributed seismic array and naturally occurring seismic sources. To approximate a linear receiver structure, stations from the seismic array and the selected earthquakes were artificially placed on the profile line by an arc-swing technique which is outlined below. This technique introduces movement in the location of the receivers along the profile because source-receiver distances are the only quantities preserved in the arc-swing method. The result is an averaging of the structure between the extremes of each station's movement and some loss of resolution of features with wavelengths smaller than this distance.

Case 1:



- The distance from 0 km on the profile to station GSM, the only station on the profile, is known and remains fixed at 68.1 km.
- Distances BC and CE are calculated with RSX recordsection plotter (source-receiver distances).
- Distance AD is determined by swinging point C to position D using an arc of curvature appropriate to a circle of radius BC. $AB+BC=AD$ now becomes the event's profile x-distance.
- $AD+CE=AG$ now becomes station YAK's x-distance along the profile. This station is NOT swung onto the profile with an arc, which would have put it at location F. Instead, the x-distance is at location G. This step is necessary to preserve CE as the source-receiver distance.
- Example: event #3 has $BD=93.6$ km which yields 68.1 km $+93.6$ km $=161.7$ km as the source's profile distance. Station YAK has $CE=36.1$ km which yields 161.7 km $+36.1$ km $=197.8$ km as YAK's profile distance.

Case 2:



- Again the distance to GSM remains fixed at 68.1 km.
- Distances BD and CD are calculated with the RSX recordsection plotter (source-receiver distances).
- The source's profile x-distance in this case is $AB+BD=AH$ by the same method as in Case 1.
- $AH-CD=AE$ now represents the profile distance of station YAK. Again, this station is NOT swung onto the line with an arc, and the source-receiver distance is preserved.
- Example: event #5 has $BD=186.1$ km which yields 68.1 km + 186.1 km = 254.2 km as the source's profile distance. Station YAK has $CD=70.2$ km which yields 254.2 km - 70.2 km = 184 km as YAK's profile distance.

It should be apparent from the two previous examples that the profile distances of the stations move according to their locations relative to the sources. The full summary of the station movement is given in Appendix III, Table A3.

In the examples for the arc-swing technique, the profile distance of station YAK ranged from 197.8 km to 184 km. Rays traced from this station to other sources will average the sub-surface structure between 184 to 197.8 km. The station with the most movement and the worst case scenario, according to Appendix III, Table A3, is station VTG.

The shaded area of Figure 4 represents approximately the area being averaged under station VTG. In a traditional profile line, each receiver has a fixed x-distance along the profile. This is impossible in this study because neither the sources nor the receivers

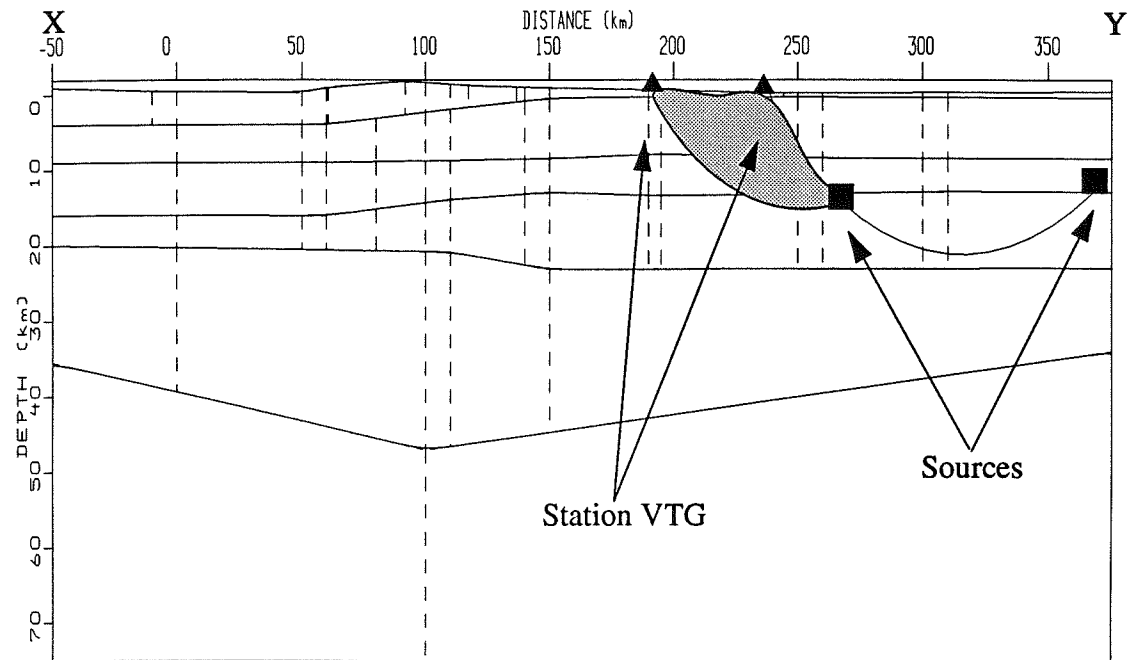


FIGURE 4. Cross-section of worst case scenario for an area being averaged. Station VTG moves from 191.1 km to 238.7 km along the profile for two separate sources. The shaded region represents the area being averaged.

scenario. The averaging is worst near the surface where raypaths are nearly vertical because the raypaths diverge to arrive at the new station location. Based on the information in Appendix III, Table A3, it seems unlikely that features with wavelengths smaller than 40 km will be resolved under the Cascades in the top 15 km. Resolution improves to 15-20 km for the Yakima Valley and then rises again to 20-25 km for the Richland area of eastern Washington.

The dataset for this study was selected based on the proximity of the epicenters to the profile and on the number of stations recording each event. A listing of the events is

worth filter which was chosen because it eliminated much of the high frequency background noise. Examples of actual arrival time picks for an event are shown in Figure 6.

One goal of the dataset selection was to extend the source-receiver distances as far as possible along the profile for each event and to have the earthquakes be well distributed over all depth ranges. This would then provide the necessary angular ray coverage needed for maximum resolution throughout the model [White and Clowes, 1990]. The goal was achieved in the Puget Sound because the subducting oceanic lithosphere [Atwater, 1970] provided hundreds of deep slab events from which to choose [Noson et al., 1988]. However, earthquakes deeper than 10 km are uncommon in eastern Washington, and data could not be gathered for source depths greater than about 14 km, thus limiting the possible ray coverage near the outer edges of the model.

Figures 7 and 8 show the proximity of the epicenters to the profile and their vertical distribution. Note the gap in the vertical distribution in eastern Washington. The zero point for the profile corresponds to event #1 in the Puget Sound in Figure 7. The entire profile extends from X, at line distance -50 km, to Y, at line distance 375 km, with an azimuth of roughly 114° and a distance of 425 km. No station corrections were applied to any of the data. The raytracing program takes into account surface topography, and local receiver structure was assumed to be small compared to anomalies that might be encountered along the raypath.

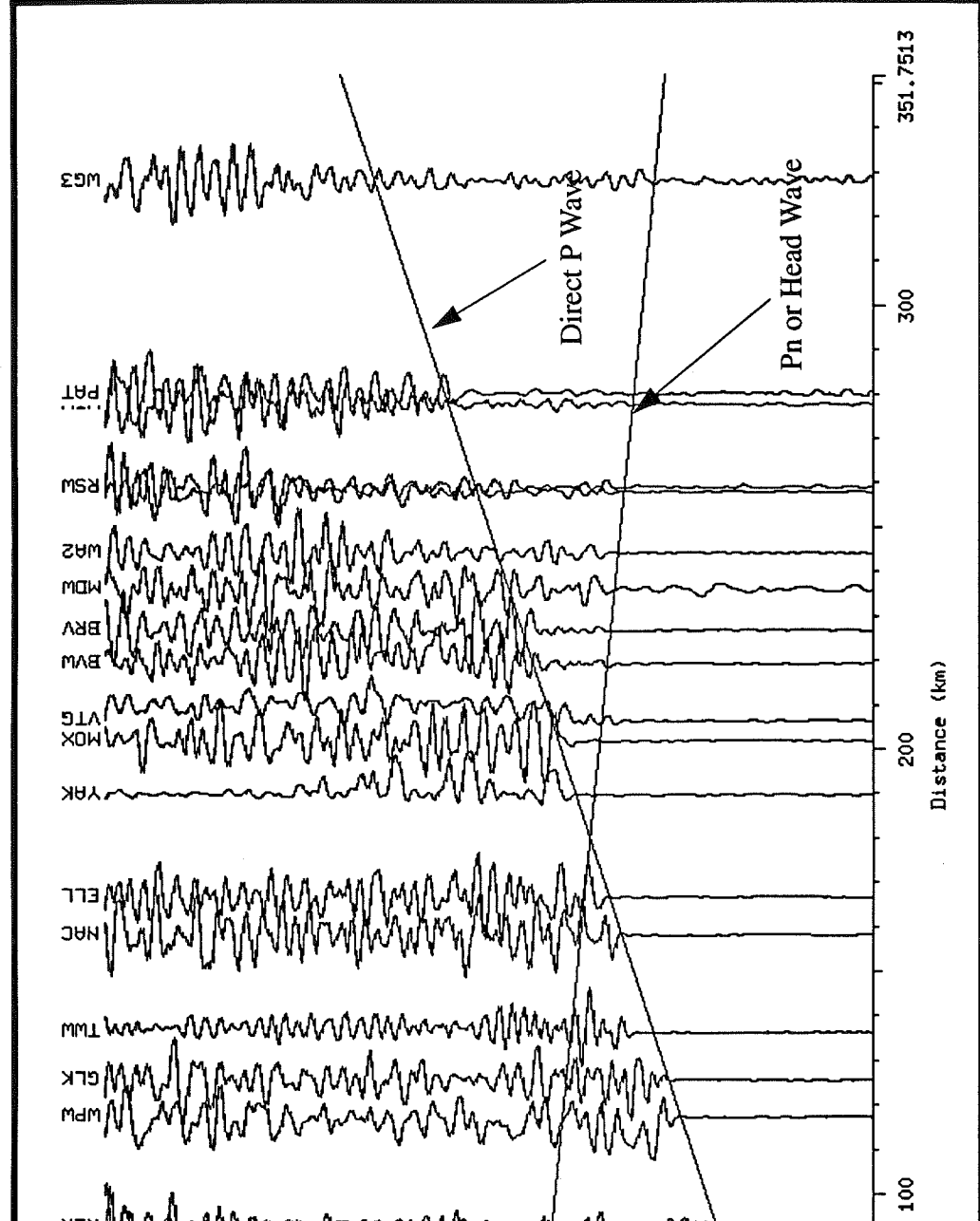
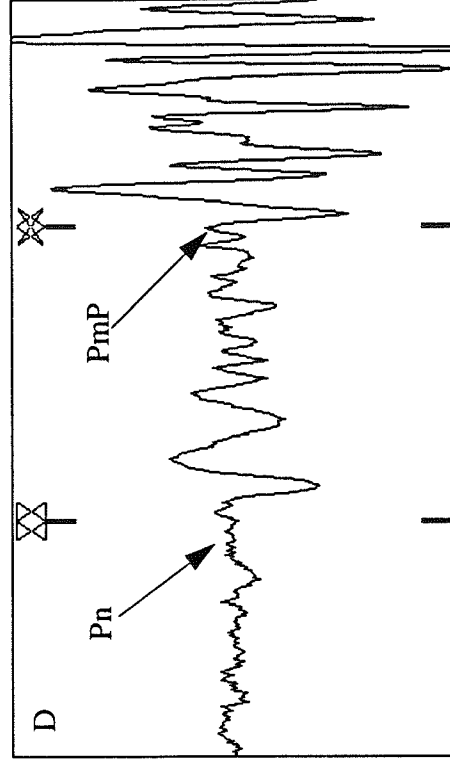
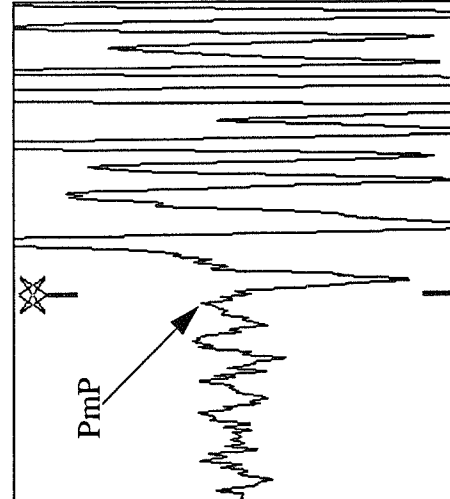
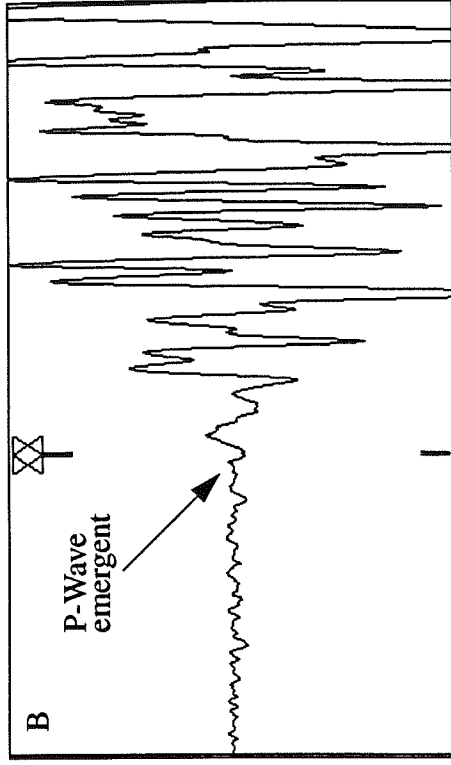
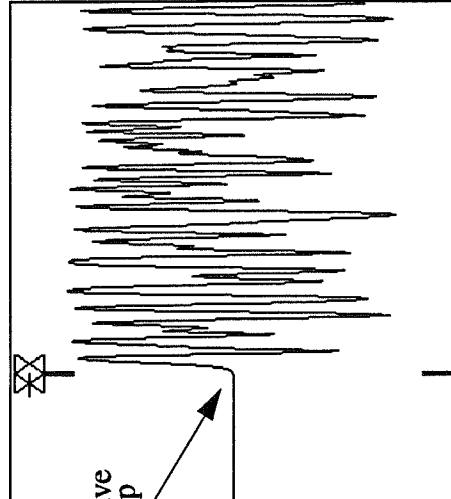


FIGURE 5. Reduced record section for event #1. Phases Pn and P-direct are marked.



Typical P picks for the data. A and B show sharp and emergent P-Waves. C and D show Pn and PmP. Uncertainties in duration. Uncertainties in pick times are not given.

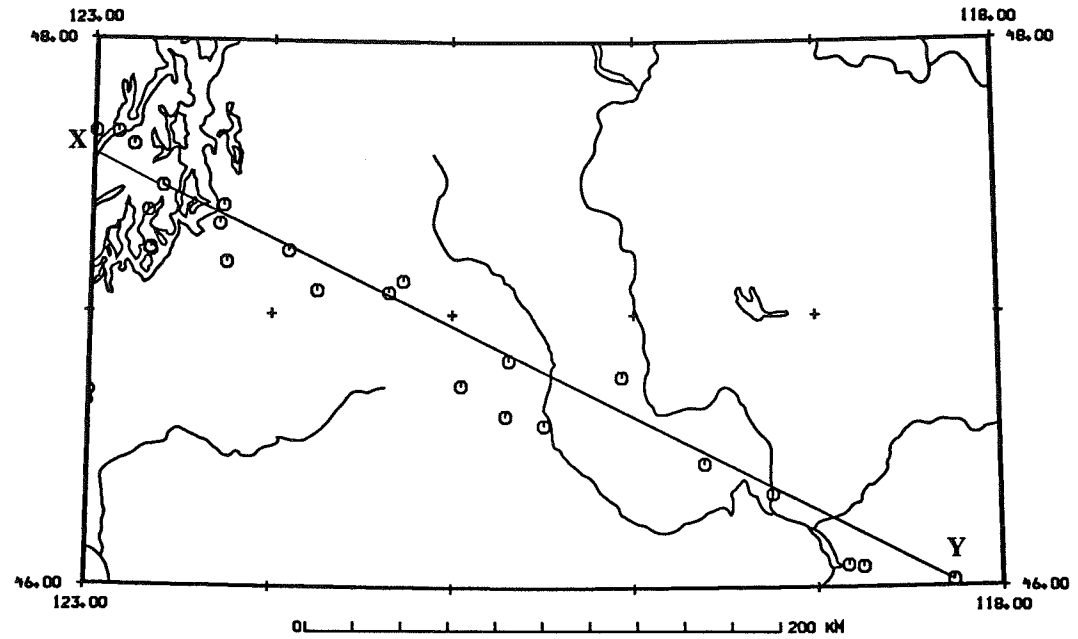
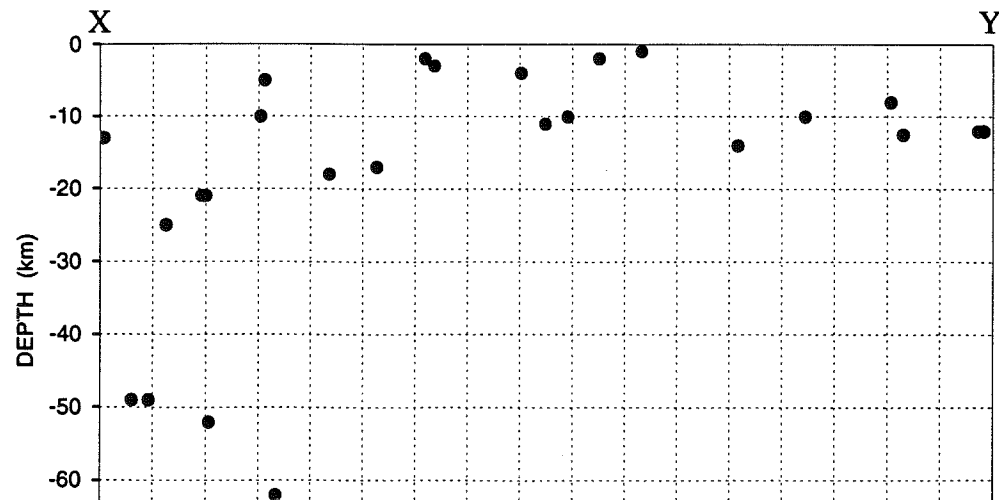


FIGURE 7. Distribution of epicenters relative to the profile line. Event locations can be found in Appendix II, Table A2.



Chapter III-- DESCRIPTION OF RAY TRACING AND INVERSION

The initial phase of this study requires that seismic travel time data be accommodated in a 2-D velocity model. An iterative approach is then necessary to improve the velocity model, and a least-squares inversion is utilized. A brief summary of the ray tracing and inversion technique used by the computer code written by Colin Zelt [Zelt and Smith, 1992] is given here.

Ray Tracing and Inversion

The velocity model is parametrized by velocity and boundary nodes to create layers specified by an arbitrary number of nodal points. Velocities within each layer are defined at the four corners of a trapezoid and are linearly interpolated between them. The trapezoid shape and the resulting velocity field can be completely general, so a minimum number of parameters is needed to represent the model fully. Rays are then traced by numerically solving zeroth-order asymptotic ray tracing equations (1) and (2) with initial conditions. θ is the angle between the tangent to the ray and the z-axis, and v is the velocity. v_x and v_z are the partial derivatives with respect to x and z .

$$\frac{dx}{dz} = \tan \theta \quad (1)$$

$$\frac{d\theta}{dz} = \frac{v_z \tan \theta - v_x}{v} \quad (2)$$

$$\Delta = \frac{\alpha v}{|v_x| + |v_z|} \quad (3)$$

Ray take-off angles are determined by an iterative shooting/bisecting method for each ray in a ray group (rays turning in the same layer). The take-off angle for a specific source-receiver geometry is determined by bracketing the receiver (source) with two rays and interpolating between these endpoints. Increased lateral variation within the velocity model usually requires an increased number of rays to be traced to ensure sufficiently accurate interpolation at the endpoints.

Velocity models that are parametrized by trapezoidal blocks tend to scatter or focus rays at points of discontinuous velocity changes in the model. To remedy the situation, boundaries with these discontinuous changes are sampled at small intervals and smoothed by applying a three-point averaging filter. Ray scattering and shadow zones are thus minimized while leaving the calculated travel times virtually unaffected.

The travel time in a continuous velocity field is given in discrete form by

$$t = \sum_{i=1}^N \frac{l_i}{v_i} \quad (4)$$

where l_i and v_i represent the path length and velocity of the i th ray segment. Since the velocity is path dependent, the problem needs to be linearized through a Taylor expansion. The result, less higher order terms, is given by

ray tracing. Δm is solved for and then applied to the current parameters. Since equation (5) is generally overdetermined, a damped least-squares approach is used. Equation (5) subsequently becomes

$$\Delta m = (A^T C_t^{-1} A + D C_m^{-1})^{-1} A^T C_t^{-1} \Delta t \quad (6)$$

where C_t and C_m represent the data and model covariance matrices respectively, and D is the scalar damping factor. The associated resolution matrix is given by

$$R = (A^T C_t^{-1} A + D C_m^{-1})^{-1} A^T C_t^{-1} A \quad (7)$$

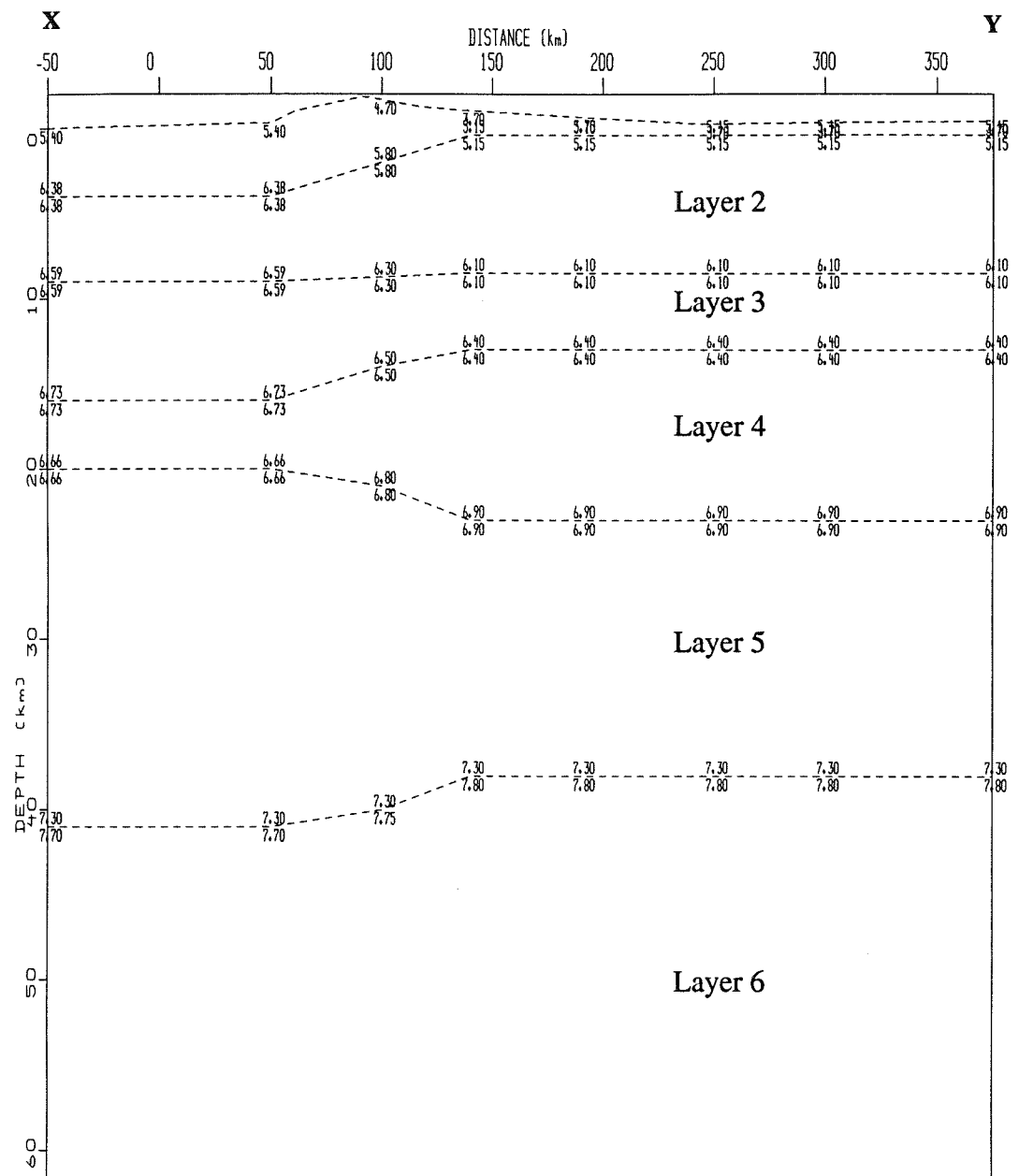
A measure of model non-uniqueness is best demonstrated by trying different starting models to see how much the parameters can vary and still produce a final model that fits the data equally well. The final models are then compared, and parameter values are bracketed.

Chapter IV -- TRAVEL TIME MODELING

The Starting Model

The initial 2-dimensional velocity model consisted of five layers. The number of layers needed and their approximate velocity and depth ranges were obtained from previous modeling efforts by Glover [1985] for eastern Washington and by Crosson [1976] for the Puget Sound. The exact starting model is shown in Figure 9. This model represents the Puget Sound model near point X and the eastern Washington model near point Y. Between the line distances 50-150 km, a linear interpolation in both velocity and depth between these two models was made. The slope of the dipping layers underlying the Cascades was a feature of the interpolation by the starting model and may not represent actual dipping structure. Each point where a velocity is specified on the model in Figure 9 represents a velocity node and an associated boundary node for a total of 153 nodes. These nodes were free to change in amplitude during the inversion step, so both the velocity and the interface structure changed. The number of these nodes and their relative spacing was determined based on knowledge of the smearing introduced by the station movement and by the minimum wavelengths of features that were expected to be visible. A 50 km node spacing seemed reasonable. The 1-D starting models by Crosson and Glover are given in Appendix IV, Table A4.

In the initial model, 305 of the possible 362 raypaths (84%) were traced. Rays are "lost" in the raytracing procedure because strong vertical and horizontal velocity gradi-

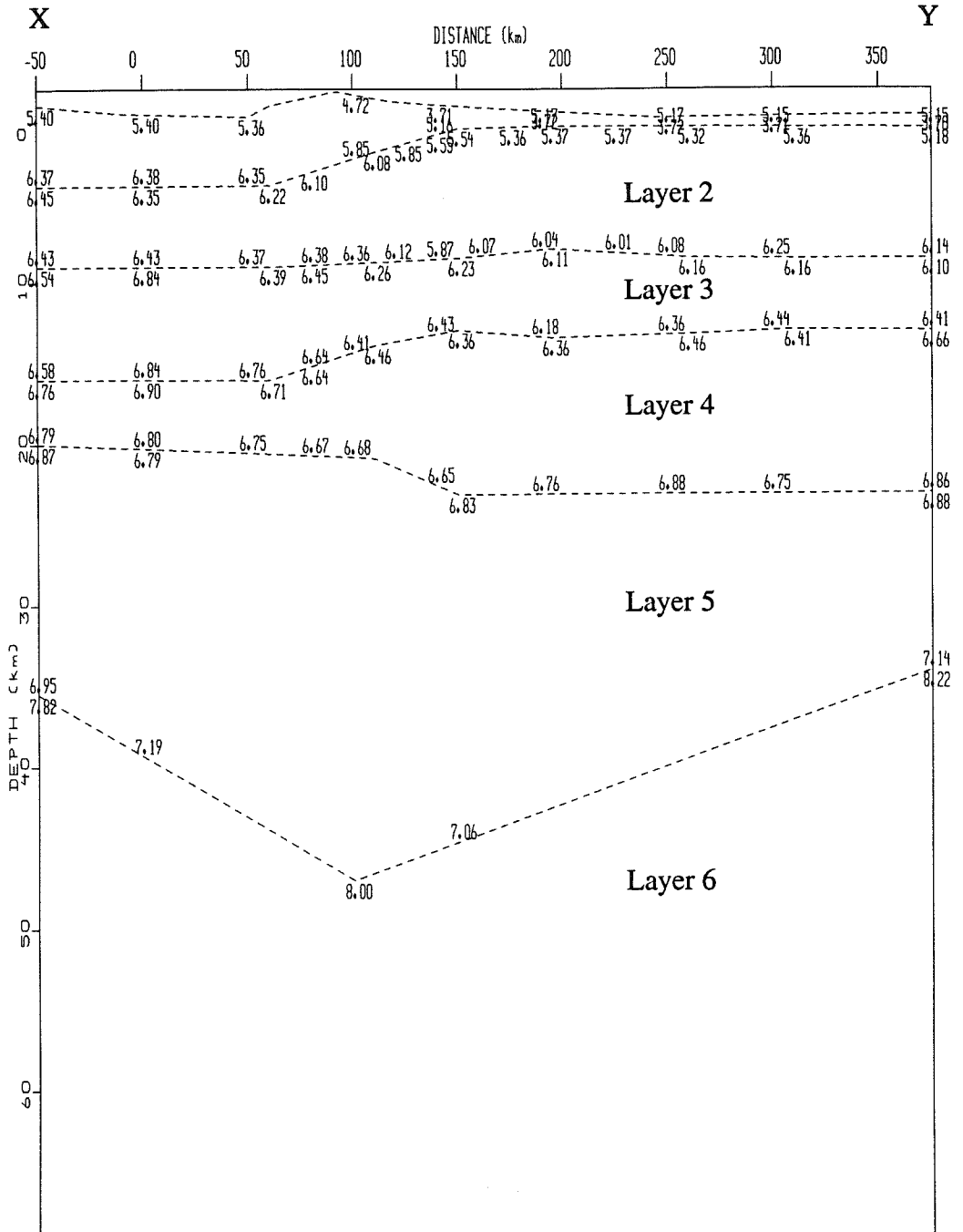


als. This represents a normalized χ^2 which should equal unity if the data fit perfectly. Therefore, considerable improvement in the model could be made.

The Final Model

The dataset of 25 earthquakes (sources) was analyzed over a profile distance of 425 km with 27 stations (receivers) recording a subset of the events. The average receiver spacing was fairly uniform and approximately 18-20 km. The final velocity model consisted of more velocity and boundary nodes in the upper three layers but a simplified structure in the lower layers and in the upper mantle. The final number and spacing of these nodes was decided during the inversion step by examining the lateral variations in the nodes. If an area exhibited extreme lateral oscillations between two velocity nodes, another node was inserted in an attempt to improve the resolution. The final model with its 135 total nodes is given quantitatively in Figure 10. A better view of the variations in the lateral velocity structure is given by a color density plot of the velocity structure in Figure 11. Much of the interface structure remained constant from the starting model, but the velocity structure within those layers changed significantly.

In the final model, 362 of the possible 376 raypaths (96%) were traced. The overall fit to the observed data was reflected in an overall RMS of 0.193 seconds for these arrivals and in a final χ^2 value of 3.375. In eastern Washington, the upper part of the final model closely resembles the model of Glover (1985). A low-density surface layer with a thickness of approximately 800 meters forms the top layer with a velocity of 3.7 km/sec.



Y

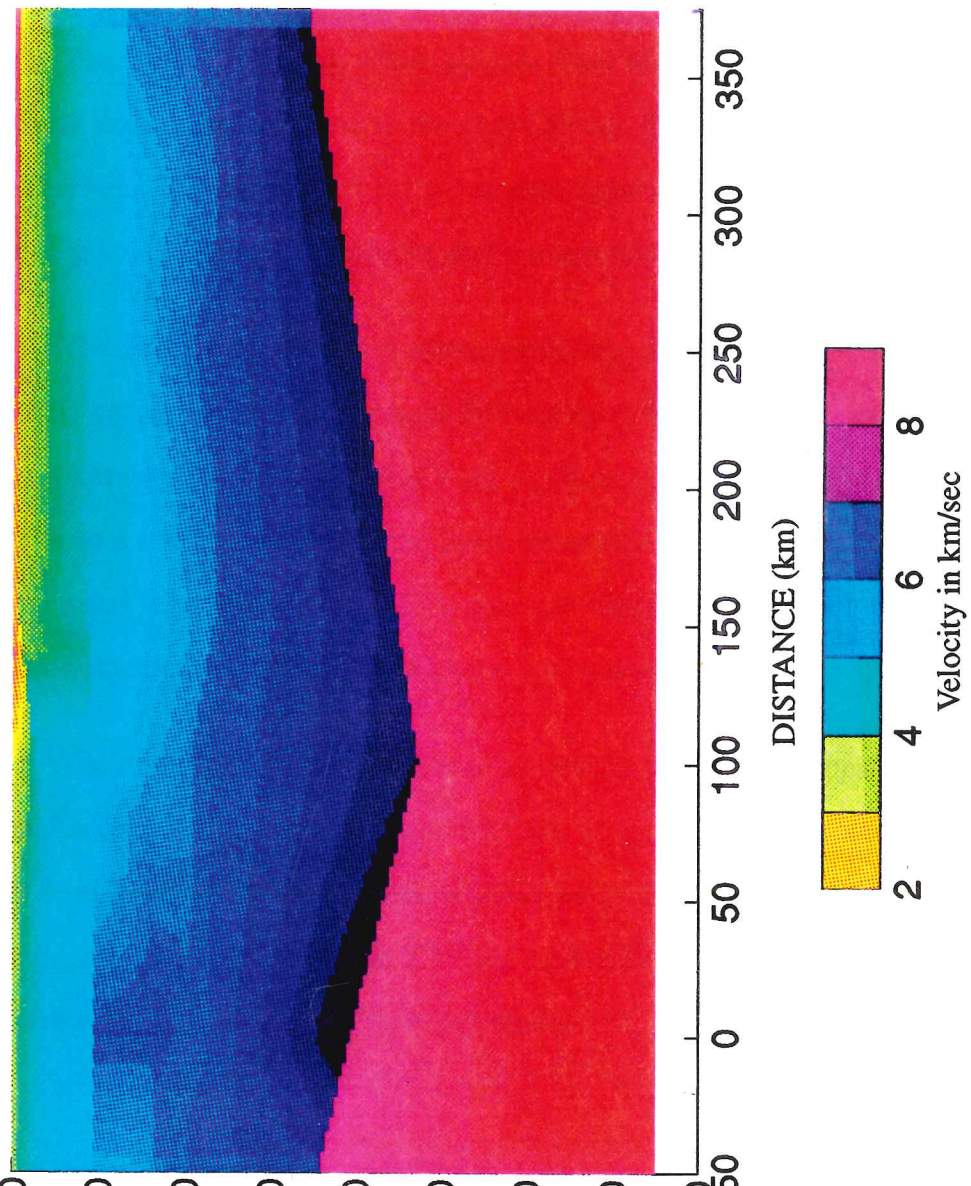


FIGURE 11. Density plot of the final velocity model. Note the apparent dip of the Moho.

locity of 7.1 km/sec. The final velocity model found lower crustal velocities of 7.14 km/sec and Pn velocities of 8.22 km/sec in eastern Washington, which are slightly higher than those found by Glover.

The Cascades Range, which extends from about 50-150 km, is characterized by relatively low crustal velocities in the upper 20 km. Note the dip in the high velocity material between 100-200 km and the subsequent upsweep between 200-300 km on the profile in Figure 11. Velocities are more uniform across the model at depths below 25 km.

The Puget Sound basin is characterized by relatively high crustal velocities and generally agrees with results obtained by Crosson (1976). Velocities range from 6.35 km/sec at 4 km depth to 6.84 km/sec at 9 km depth near $x=0$ km along the profile. There appears to be a small velocity reversal under the central Puget basin at 16-20 km depth, and lower crustal velocities of 6.95-7.19 km/sec are slightly higher than those found by Crosson. Pn velocities in the Puget Sound were 7.82 km/sec at a depth of 35.5 km.

The most notable feature in the final velocity model is the apparent dip of the continental Moho. It starts at a depth of 35.5 km in the Puget Sound, increases to a maximum depth of 47 km under the central Cascades, and ends at a depth of 34 km in eastern Washington. The apparent dip is 2.7° for eastern Washington, dipping to the west, and 4.4° for western Washington, dipping to the east.

Chapter V -- DISCUSSION OF TRAVEL TIME MODELING

The number of refraction studies that cross the high Cascades is very limited. Johnson and Couch (1970) had only 15 stations for a single-ended profile line of 500 km length. Therefore, their ability to resolve details of crustal structure was more limited than is the case in this study. In addition, their profile was located considerably further north. To interpret my results, I will rely mostly on data and conclusions from this study as well as some other well-established parameters, such as Pn velocities, determined by other investigators.

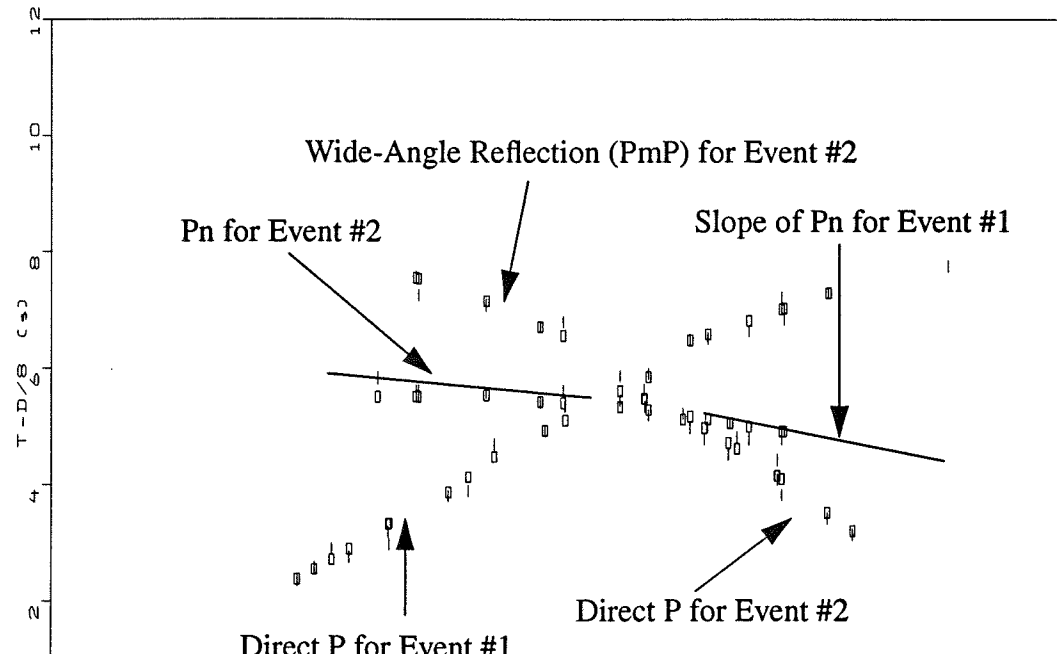
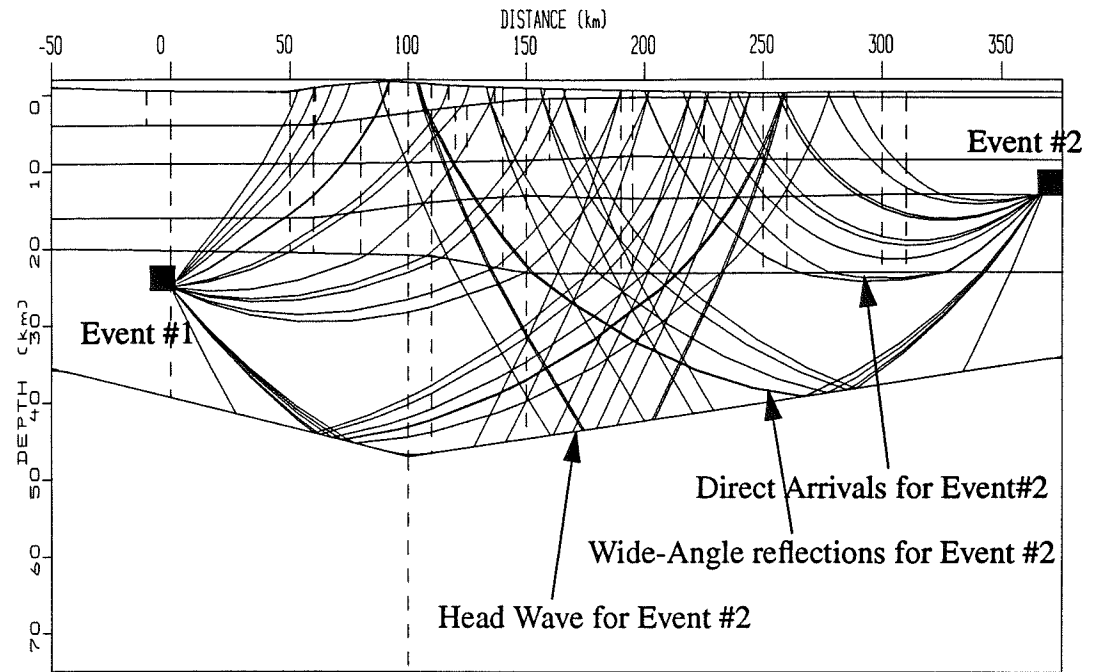
Figure 11 shows relatively low velocities directly under the Cascades at depths of 10-25 km. This feature is large enough to be detectable by the resolution of the method, so it is likely to be real. The data should be adequate to resolve the change from the eastern velocity regime to the Puget Sound regime. The number of velocity nodes was increased in layers 2, 3, and 4 to resolve this transition structure. A total of 48 velocity nodes are present in layers 2 and 3 combined. At $x=80$ km and a depth of 9-16 km, velocities are closer to those found in eastern Washington. However, this feature could be an artifact of the starting model and the linear interpolation between the two 1-D starting models. The exact extent of the starting model influence in this region is not known. Johnson and Couch (1970) found insufficient evidence to support the theory of a root based on their refraction line which crossed the northern Cascades above the Canadian border, but resolution in their experiment was limited.

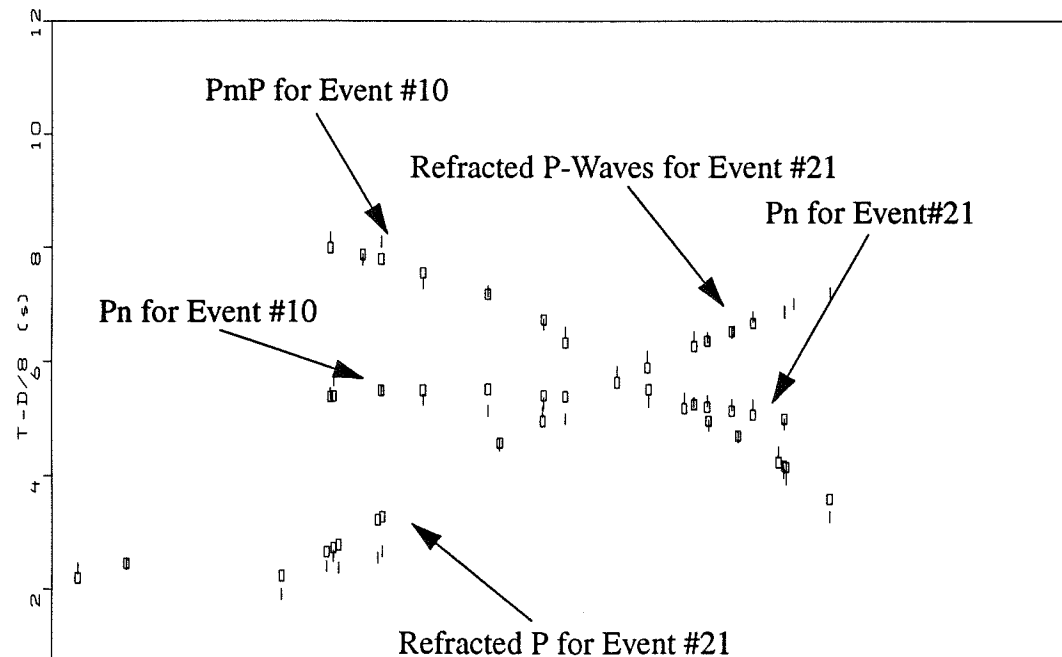
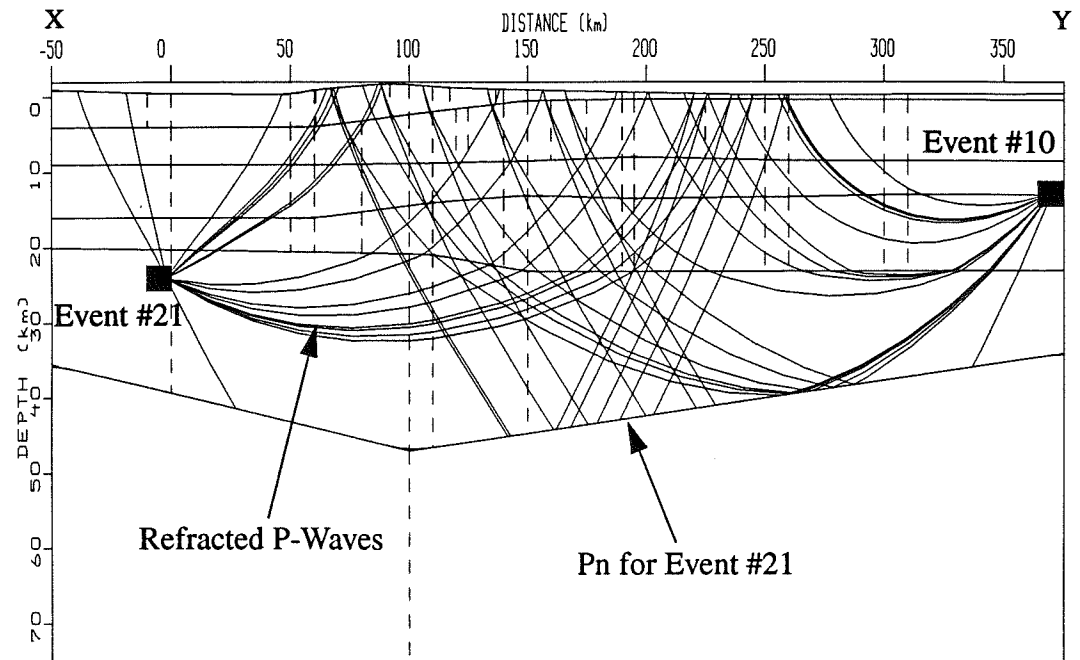
3.2° respectively by Zervas and Crosson (1986). The added constraint provided by reversed profiles lends strength to these features of the model.

The dip of the Moho is strongly constrained by the slopes of Pn arrivals on reduced travel time curves. Pn data are sensitive to the geometry of the interface but not to its absolute depth. On the other hand, the absolute depth of the Moho is constrained well by PmP phases. PmP phases are sensitive to the depth but not as strongly to the interface dip. Thus we need to model both Pn and PmP simultaneously in the final model. Travel times can be accommodated either by increasing velocities or by shallowing the depth. Modeling both phases provides constraints on the range of this trade-off. Two separate, independent measurements of the apparent dip of the continental Moho are given in Figure 12 and Figure 13. These figures show the raytracing of the relevant phases through the final velocity model with two events shown on each figure. These events represent points near the extremes of the profile and essentially cover the entire profile along both directions.

In Figure 12, Pn arrivals from Event #1 have a higher apparent velocity traveling from west to east than do the Pn waves from Event #2 traveling from east to west. There are two possible end-member explanations for these observations: (a) the upper mantle has a lateral increase in velocity from west to east, or (b) the Moho interface dips to the west at a shallow angle.

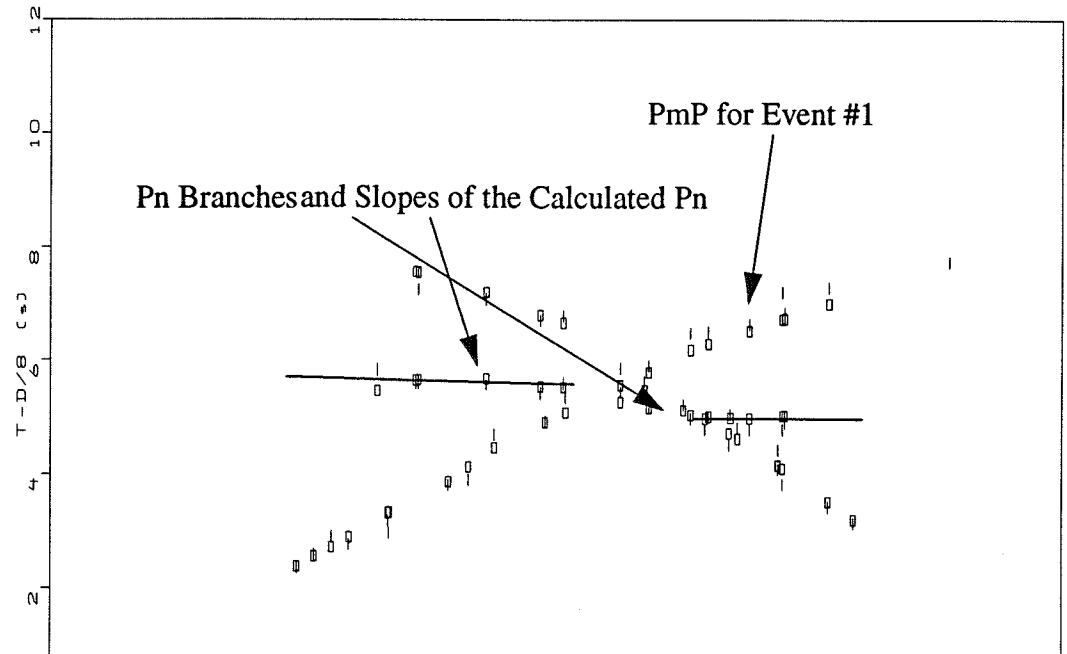
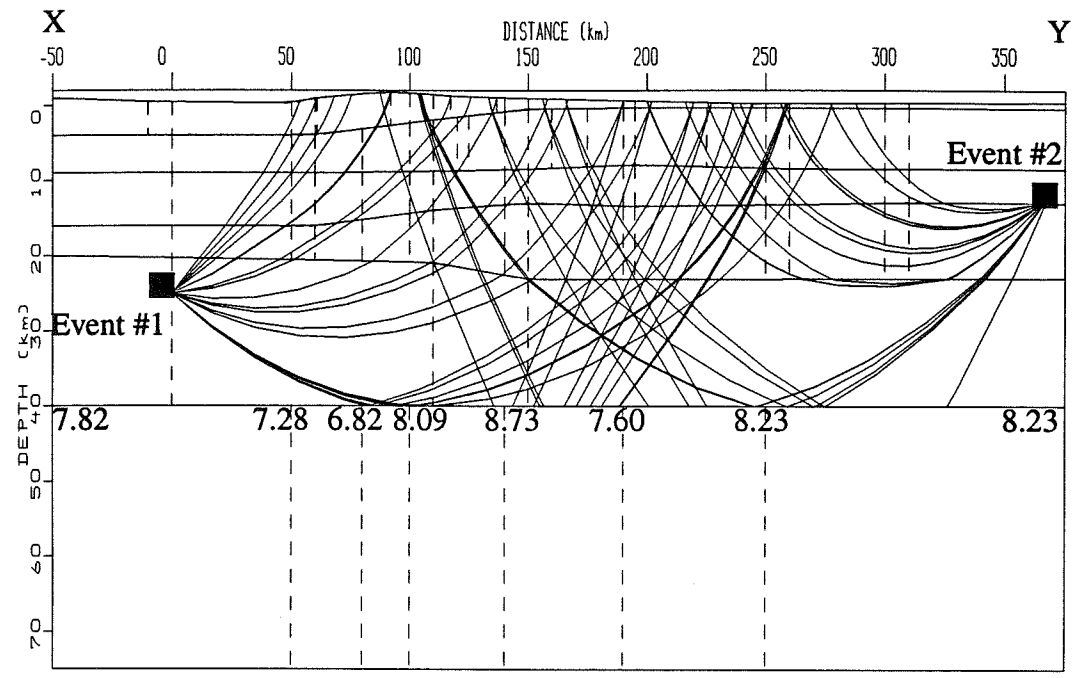
Since both are plausible answers, a separate model was created to test the lateral





depth of 40 km. Several inversion steps were then performed with minimal damping, and the velocities were allowed to vary to accommodate the observed traveltimes differences. The a priori assigned variances were $\sigma_v = 0.20$ km/sec for the velocity nodes, and $\sigma_z = 1.0$ km for the boundary nodes. The boundary nodes were kept fixed throughout this particular inversion. In the result of the inversion, the final velocities in the upper mantle ranged from 6.82 km/sec to 8.73 km/sec. Figure 14 shows the rays traced through the model and the reduced traveltimes curves. The only differences between this model and the previous model are the flat Moho interface, which is now fixed at 40 km depth, and the velocities and lateral gradients in the upper mantle. With the flat Moho model, it was possible to trace 362 of 376 rays, giving an overall RMS=0.217 seconds. Comparing the χ^2 value of 4.5 for the flat Moho model with the value of 3.37 for the dipping Moho model, an F-test suggests that the dipping Moho model is significantly better.

From visual inspection of Figures 12 and 14, the fit to the observed data and to a linear slope for Pn is better for Figure 12. Rays traveling from west to east have a higher apparent velocity and a correspondingly different slope than those traveling from east to west. The flat-layered model was not able to model this observation, even with the introduction of radical lateral gradients, which leads to the conclusion that the dipping interface model fits the observations best. In addition, Pn velocities derived for the flat-lying model are higher than can be accounted for by upper mantle intrinsic velocities. Pn velocities for the dipping model are consistent with previous studies by McCollom and Crosson (1975), Zervas and Crosson (1986), and Catchings and Mooney (1985).



phases usually large in amplitude and easily identifiable. Sample PmP phases are shown in Figure 6, parts C and D. PmP phases are especially sensitive to the depth of the reflective interface. Increasing the depth to that interface would increase the travel times and would be detectable in the residuals. Figures 12 and 13 show an acceptable fit of PmP to the observed data, while Figure 14 shows considerable misfit for the PmP observations from Event#1. The calculated times are too early, which implies that the depth to the interface is too shallow. One way to remedy this discrepancy is to decrease the velocity in the lower crust. However, this is not warranted based on observations from other refracted phases. Another possibility would be to increase the depth of the interface. However, this would decrease the quality of the fit of the Pn branches. The result is that the flat-interface model cannot adequately model both the PmP and the Pn observations simultaneously. Hence the dipping model is superior and is adopted as the final model for this study.

Comparison With Gravity

The depression of the upper mantle and the Moho indicated in the final velocity model should be visible in the gravity signature on the Earth's surface. Dense mantle material is displaced by less dense crustal material, and the resultant gravity signal should show a large negative Bouguer anomaly. Data compiled by Danes (1969) and by the Complete Bouguer Anomaly Map [Bonini *et al*, 1974] reduce Washington regional gravity to sea level and apply terrain and elevation corrections. The resulting values for the

Danes (1969) reflect the mass excess or deficiency under the collection site. In the

A first-order calculation for the surface gravity anomaly caused by the depressed upper mantle can be represented by a perturbation to gravity caused by an infinite buried slab with a constant thickness and a given density contrast. This would then represent the upper bound on the gravity anomaly since the slab produces a larger anomaly than a triangular root. Turcotte and Schubert (1982) derive the expression of an infinite buried slab with a density contrast $\Delta\rho$ and a thickness H as

$$\Delta g = 2\pi G\Delta\rho H \quad (8)$$

where $G = 6.67 \times 10^{-11} \text{ Nm}^2 \text{ kg}^{-2}$ is the gravitational constant. The thickness of the slab corresponds to the depression of the Moho from its unperturbed equilibrium state. Density contrasts between the lower crust and the upper mantle probably range from 300-450 kgm^{-3} . Applying equation (8) I derive $\Delta g = -150$ milligals for the lower extremes in $\Delta\rho$ and $\Delta g = -225$ milligals for the upper extremes in the case of a 12 km thick slab. These numbers are negative because the crust is less dense than the mantle and $\Delta\rho$ is negative. For this slab thickness, a density contrast of 300 kgm^{-3} seems to be somewhat high to explain the observed Bouguer anomalies. Thinning the slab to 10 km with the same density contrast yields $\Delta g = -125$ milligals. While this number is more in agreement with the observed values, it also illustrates the trade-off between the thickness of the slab and the density contrast across the Moho. The upper limit of 450 kgm^{-3} results in a slab thickness of 7 km for an anomaly of -132 milligals.

As discussed earlier, Pn and PmP arrivals constrain the depth to the Moho and the

the slopes of Pn curves on the reduced travel time plot of Figure 12 need at least 10-12 km of depression over the length of 275 km along the Moho in eastern Washington to offer the best fit to the observed data. Thus a density contrast of around 300 kgm^{-3} or less would seem to be indicated.

A Moho depression of 12 km beneath the high Cascades is reasonable and can be modeled effectively to first order with a simple buried slab approximation. Density contrasts between the lower crust and the upper mantle above about 300 kgm^{-3} are possible but unlikely in view of the constraints placed on the minimum thickness of the Moho depression.

Resolution and Variance

Initially, the dataset was not particularly stable for inversion calculations. The final model contained 135 nodes and 376 observed raypaths, which meant that it was overdetermined by a 3:1 ratio. Traditional refraction profile experiments are typically overdetermined by ratios of 10:1 or more [Zelt and Smith, 1992, Gridley, 1993]. Several steps were taken to obtain a stable, convergent inversion solution.

First, the traveltimes residual mean was removed from each event so that no individual event would force the solution in one particular direction. A large mean for one event could introduce unrealistic changes into one area of the model that could not be accommodated by the rest of the data. Figure 15a shows the residuals of all traveltimes to the observed data in the starting model, and Figure 15b shows the same for the final ve-

gin time and depth, and many of the events were perturbed in both parameters to achieve the best fit possible.

Next, a pseudo-Jackknife method was employed to identify areas of the model that were particularly unstable for each event. A good account of the Jackknife method is given by Lees (1989). Since the solution had not converged on a best-fit solution, a true Jackknife method was not possible. The idea in the pseudo-Jackknife method was to leave out the i -th event, iterate once on a dataset without this event, observe the new model and subtract it from a reference model. This process was repeated with each of the models derived from the first pseudo-Jackknife iteration. The resulting set of models now consisted of a set of difference-of-differences for each velocity and boundary node. If all events had the same effect on the model, these values should all be zero. Areas of the model that were particularly unstable were identified, and the corresponding velocity nodes were kept fixed throughout the inversion.

The final assumption to stabilize the inversion was that boundary depths were more or less known in all areas except directly beneath the Cascades. Boundary nodes in the range 50-150 km were allowed to vary in the first few iterations, but the damping was kept high. No boundary nodes were modified in the final inversion step. The total number of nodes modified in the final model was 54.

There is an inherent trade-off between resolution and variance. High resolution generally means larger variances and vice versa. Menke (1984) describes a process

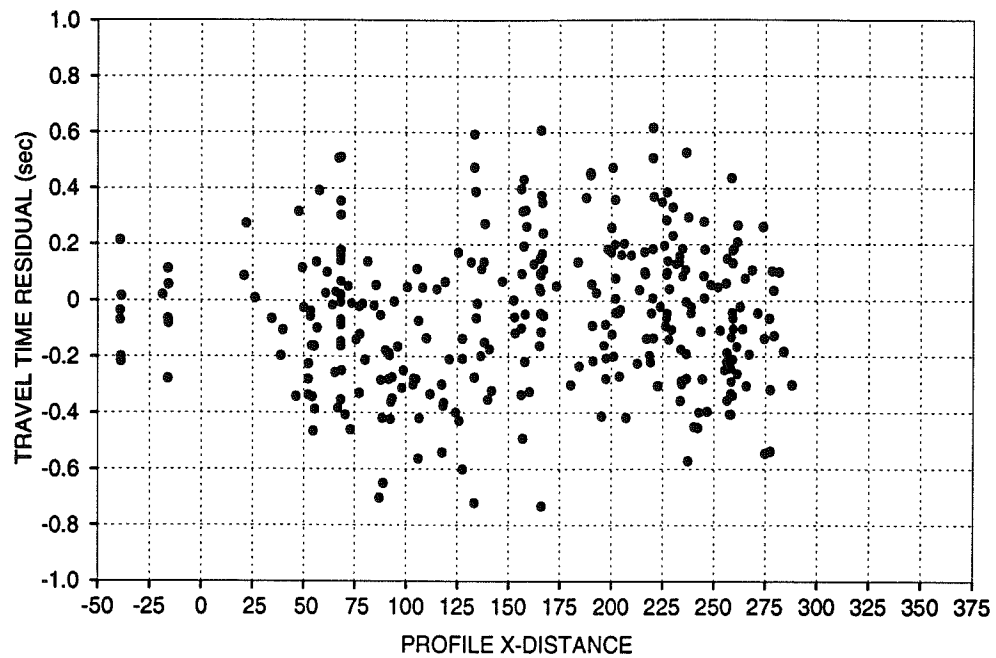
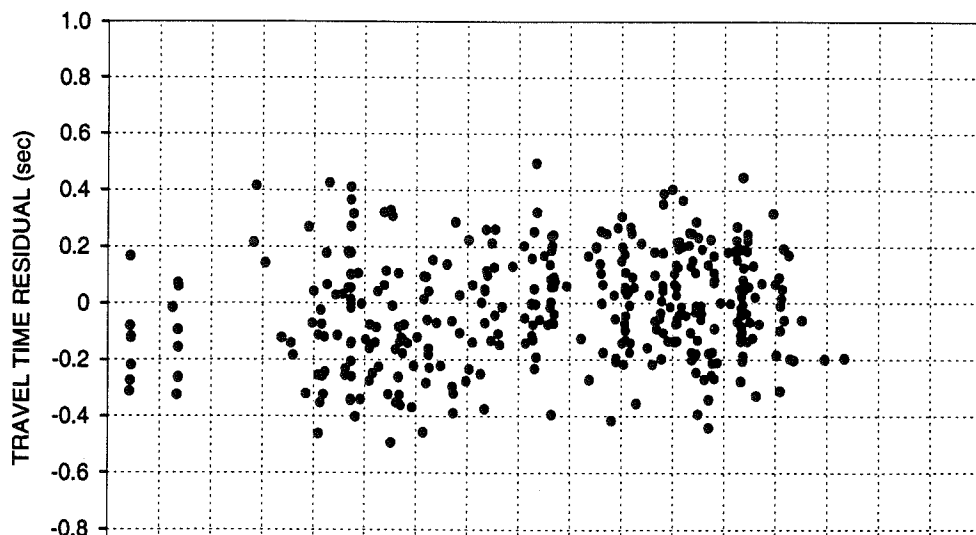


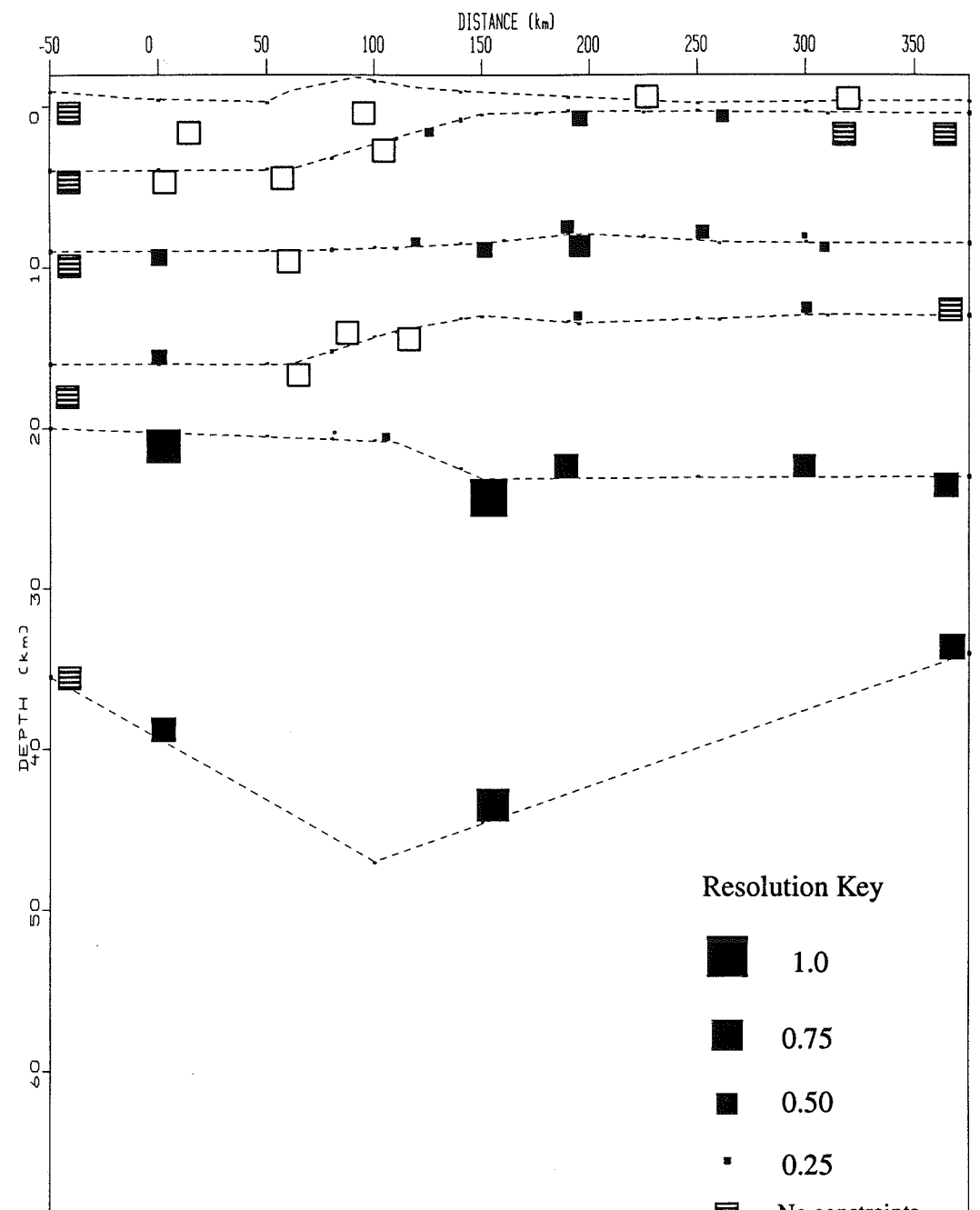
Figure 15a. Travel time residuals for the starting model. Zero mean.



same for all picks and were estimated at $\sigma_{tt} = 0.1$ sec. for an average pick. The minimum damping required for a stable, converging solution was found to be $D=10$. This factor represents the scalar value in equations (6) and (7) and is a measure of the amount of change allowed in the model per iteration. Small damping factors caused too much instability by allowing large changes, while damping factors greater than $D=100$ suppressed any significant changes in the model parameters. A complete account of the resolution values and the standard errors for the velocity nodes is given in Appendix V, Table A5.

A comparison of resolution values between parts of the model is shown in Figure 16. Perfect resolution means that the model can accurately resolve both the size and the amplitude of a subsurface feature. Typical resolution in layers 1, 2, and 3 is only 25-50% of what it is in the lower layers. However, the variances for this damping factor are quite small. Since boundary nodes were fixed during the inversion, no variances or resolution values were calculated for those nodes. Open squares represent areas where the velocity nodes were also fixed during the inversion because of apparent instabilities in the model identified through the pseudo-Jackknife method. Variances calculated for the velocity nodes range from $\sigma_v = 0.09$ to 0.20 km/sec, with the higher variances generally corresponding to the worse resolutions.

Figure 16 shows the diagonal elements of the resolution matrix calculated during the inversion via equation (7). Figure 16 is a good indicator of the relative resolution between nodes in the model. Without the entire $N \times M$ resolution matrix, the spread of the resolution is unknown. In other words, the amount of information "leaked" from one



entially parallel are unable to provide independent information. The geometry of most surface-surface refraction experiments restricts them from having the necessary angular ray coverage at depth to keep resolution high, even with dense receiver spacing. This study, however, utilized data occurring at depth which should increase the angular ray coverage at lower crustal and upper mantle depths.

A particularly useful tool for resolution analysis is a visual assessment of the actual ray coverage for an area. An insufficient numbers of rays sampling any given area in the model will give rise to unconstrained velocities, and fictitious structure that is not apparent in the data can be introduced into the model. Figure 17 shows the actual ray coverage for the final model in this experiment. There is sufficient angular ray coverage in all crustal layers to ensure maximum resolution due to sampling all the regions of the model. Areas with limited ray coverage also only have a limited number of nodes.

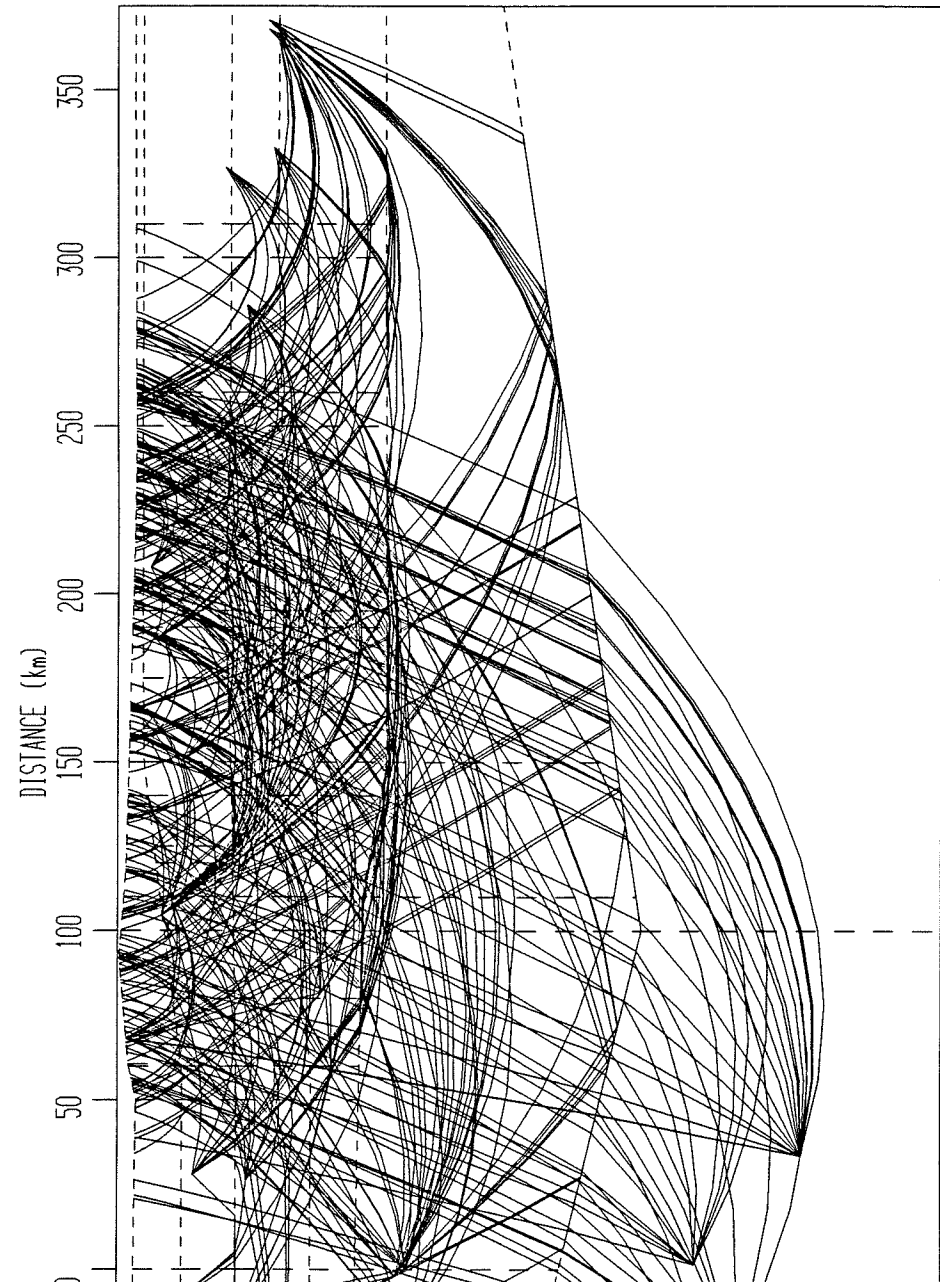


FIGURE 17. Ray coverage of the final velocity model. Only observed phases are traced.

Chapter VI -- REFLECTIVITY SYNTHETICS

The purpose of computing synthetic seismograms via the reflectivity method was to test the sharpness of the Moho boundary interface. It should be possible to determine whether the Moho interface represents a discrete boundary or whether it consists of a transition zone of some finite thickness by modeling the waveforms of Pn and PmP phases.

The reflectivity method is used to compute synthetic seismograms for a plane layered model consisting of a stack of homogeneous layers [Mueller, 1985, Mallick and Frazer, 1987]. The source is specified with either a complete moment tensor or by specifying the moment, dip, rake, azimuth to station, and azimuth of the fault plane. The resulting synthetic seismogram represents a complete solution of all reverberating rays at a particular receiver location. The synthetic output is a broadband signal and cannot be compared to the short-period signal from the real data directly until it has been convolved with the short-period instrument response from a particular network station. The real and the synthetic seismograms should look similar with respect to major packets of arriving energy if the velocity and source models are approximately correct. Although the reflectivity method represents a complete solution, it still only approximates the real Earth structure by a stack of homogeneous layers which cannot model lateral variations in velocity.

The receiver chosen for this experiment was station ELL. The event chosen for

The 1-D velocity model in Figure 18 was used to approximate the final velocity model. It consisted of six homogeneous, flat-lying layers of constant velocity and density overlying the upper mantle. The 1-D model approximation is a limitation imposed by the reflectivity method, thus lateral inhomogeneities cannot be considered. The source-receiver pair was kept in eastern Washington where a 1-D approximation to the velocity model was estimated to be most reasonable.

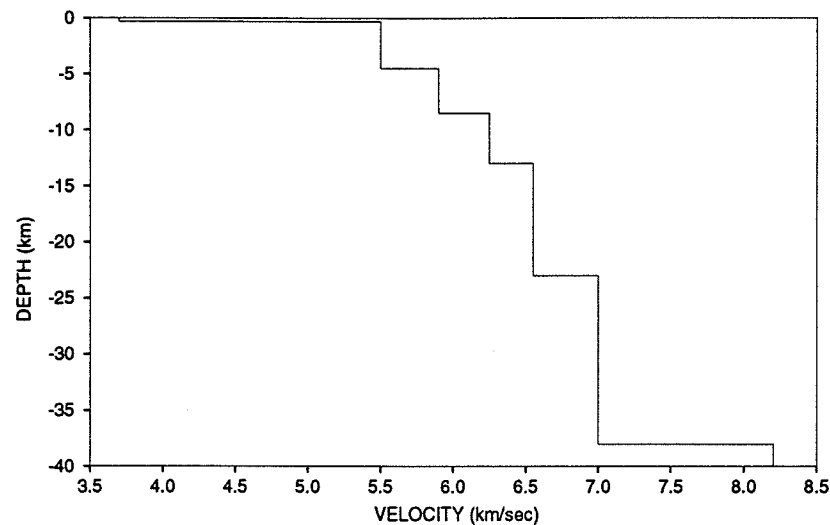


FIGURE 18. 1-D velocity model used to calculate the synthetics.

In order to identify discrete phases on the synthetic seismograms, theoretical travel times for the 1-D model were calculated using the ray tracing code in the forward modeling mode. At a source-receiver distance of 200 km, Pn was calculated to be the first arriving wave energy, followed by PmP at about 1.3 seconds after the Pn arrival.

proximation $v_p = \sqrt{3}v_s$. The amplitudes of arriving phases depend on the attenuation factor Q , defined as the loss of energy per cycle. $Q_\alpha = 600$ and $Q_\beta = 300$ were assumed for P and S waves respectively.

The source mechanism calculated from first motion data for Event #2 was: seismic moment= 1.0, dip= 38° , rake= -65° , azimuth of fault plane= 80° , azimuth of receivers= 294° . However, Event #2 was located on the eastern edge of the Washington Regional Seismic Network (WRSN), and there existed a large azimuthal gap in station coverage which could introduce substantial error in the source mechanism solution.

Filtering for the real data was performed with a Butterworth low-pass filter of appropriate order for a corner frequency at 10 Hz and a sharp decay by 50 dB to 12 Hz. This left sufficient signal for a comparison but eliminated the higher frequency background noise. The synthetics contained energy up to about 10 Hz as well. The traces were then aligned corresponding to the origin time of the event, and the waveforms were compared. Figure 19 shows the overall comparison of the waveforms.

Discussion

The initial objective of computing reflectivity synthetics was to correlate reflected phases on the real and the synthetic data in order to verify the depth to these reflective interfaces. In theory it should be possible to correlate high-energy phases, like PmP, between the real data and the synthetic. However, it is obvious from Figure 19 that there are no phases with exceptionally high amplitudes in the real data, and the entire wave-

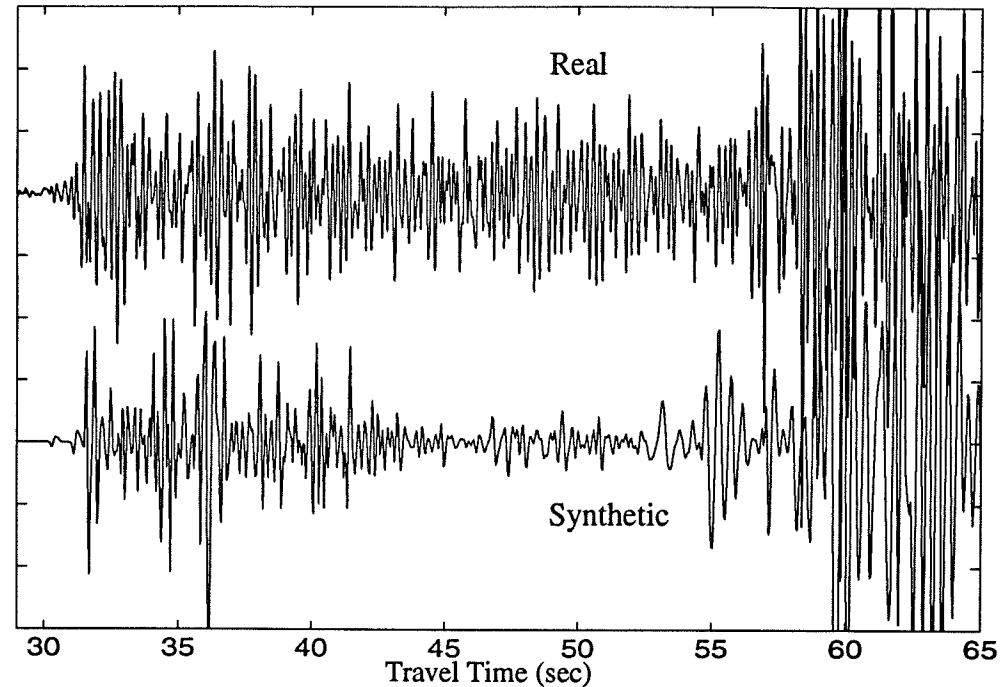


FIGURE 19. Comparison of the full waveforms for the synthetic and the real data. Synthetic data is on the bottom and the real data is on top.

The absence of strong reflective phases might be caused by subsurface structure. Station ELL is located on the northern side of Manastash Ridge on the Grande Ronde basalt of the Columbia River Basalt group [Walsh *et al.*, 1987]. These basalts scatter significant seismic energy during surface-surface refraction experiments [Shirley, 1984] and keep energy from reaching subsurface layers, so by reciprocity the opposite might be true here. Subsurface energy is unable to reach the surface because it is reflected off the underside of the basalts and reverberated in the layers themselves. This scattering of energy may explain why large peaks are not visible in the real data. Pn and PmP should be

It might be possible to obtain information about the sharpness of the Moho interface, however, because this sharpness should manifest itself in a characteristic amplitude ratio between P_n and P_mP . A discrete interface would yield a relatively low P_n/P_mP ratio because P_mP represents a very strong reflection. If the interface structure is a transition zone of finite thickness, this ratio should increase. It should be possible to model such a transition zone and compare it to the observed P_n/P_mP ratio.

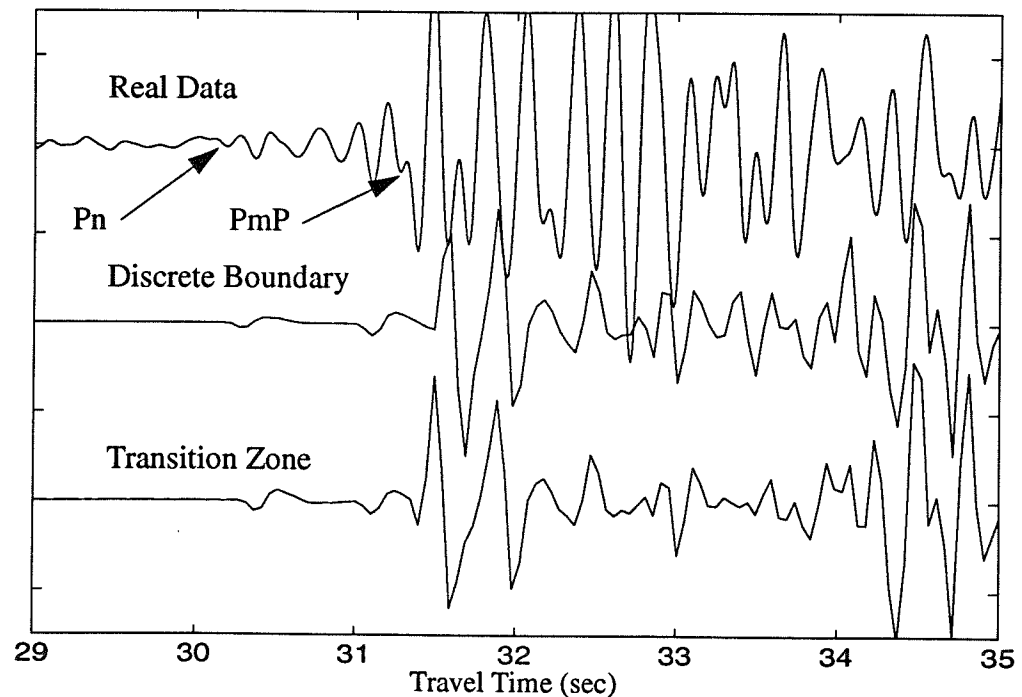


FIGURE 20. Comparison of the first 16 seconds of the real data and synthetics composed of a.) a model with a discrete interface and b.) a model with an 8-layer boundary spread over a 4 km thick transition zone.

Figure 20 shows a comparison between the real data and two separate models.

Pn/PmP ratio that more closely approximates the ratio found in the observed data in the top trace. The amplitude of Pn is enhanced relative to PmP.

It is unclear from the evidence presented exactly how thick the transition zone is, but Figure 20 shows that a transition zone model yields a more realistic Pn/PmP ratio than does the discrete boundary model. With further work, it should be possible to obtain more accurate estimates of the transition zone thickness from the waveform modeling, but this study only focuses on first-order effects, i.e. the Moho is not likely to be a discrete boundary. Further modeling efforts might include a more accurate amplitude modeling in a region which is not underlain by basalt, such as western Washington, to determine the influence the basalts have in eastern Washington. Real data waveforms from this region might also make correlation of phases possible, and the depth to the boundary interfaces and their impedance contrasts could be established. For completeness, an entire array of stations at various distance and azimuth ranges should be modeled with synthetic seismograms to distinguish local and regional site effects.

Reflectivity synthetic modeling could emerge as a powerful tool in modeling the structure of the Moho, but this study is limited by the interference of near-surface structure in the observed waveform. The modeling efforts of this study represent the first step in determining the structure of the Moho transition zone.

Chapter VII -- CONCLUSIONS

This study determined a 2-D velocity model that consisted of five crustal layers overlying the upper mantle. Velocities in the upper crust were generally higher in the Puget Sound region than in eastern Washington, but this contrast disappears below 25 km depth. The reflectivity modeling suggests that the Moho interface in eastern Washington tends to be more transitional in nature, rather than discrete. The Moho was determined to be a dipping interface with 2.7° dip to the west in eastern Washington and 4.4° dip to the east in western Washington. The depth to the Moho interface was 35.5 km in the Puget Sound, 34 km near Walla Walla, and 47 km at its maximum under the high Cascades.

The general shape and depth of the Moho interface were established and constrained by the combination of Pn and PmP phases. If velocities in the upper mantle were kept fixed, changes as small as ± 1 km in the maximum thickness of the crust were detectable by the travel time residuals. The shape of the Moho was better determined in eastern Washington because of Pn phase constraints. The deep sources in the Puget Sound helped constrain the western part of the Moho. Reversibility of the profile was also shown to be important in constraining the Moho geometry.

Pn observations required at least 12 km of depression over the 275 km profile length in eastern Washington to fit the observed travel times accurately. A first-order gravity calculation based on a 1-D buried slab approximation and a comparison with the

This study has shown that it is possible to determine a 2-D velocity structure across an region using only natural sources and an already existing seismic network. There are limitations to the resolution in the upper layers, but much important information can be obtained, like the depth and the geometry of the Moho. There are also some advantages, like having deep sources that contribute to the angular ray coverage at depth. Adding gravity measurements and calculations of synthetic seismograms places further constraints on the velocity model and yields a more robust final result.

Bibliography

- Atwater, T., Implications of Plate Tectonics for the Cenozoic Evolution of Western North America, *Bulletin of the Geological Society of America*, **81**, 3513-3536, 1970.
- Bonini, W.E., Hughes, D.W., Danes, Z.F., Complete Bouguer Gravity Anomaly Map of Washington, Geologic Map GM-11, Washington State Department of Natural Resources, 1974.
- Catchings, R.D., and Mooney, W.D., Crustal Structure of the Columbia Plateau, Abstract in *Earthquake Notes*, **55**, No. 1, 22, Eastern Section of the Seismological Society of America, 1985.
- Cowan, D.S., and Potter, C.J., Continent-Ocean Transect B3: Juan de Fuca Spreading Ridge to Montana Thrust Belt, The Geologic Society of America, Inc., 1986.
- Crosson, R.S., Crustal Structure Modeling of Earthquake Data 2. Velocity Structure of the Puget Sound Region, Washington, *Journal of Geophysical Research*, **81**, 3047-3054, 1976.
- Danes, Z.F., Gravity Results in Western Washington, *Transactions of the American Geophysical Union*, **50**, 548-550, 1969.
- Glover, D.W., Crustal Structure of the Columbia Basin, Washington from Borehole and Refraction Data, *Masters Thesis*, University of Washington, 1985.
- Gresens, R.L., Geology of the Wenatchee and Monitor Quadrangles, Chelan and Douglas Counties, Washington, *Bulletin Washington State Geology and Earth Resources Division*, **75**, 1983.
- Gridley, J.M., Crustal Structure of Western Washington State. *Ph.D. Dissertation*. Univer-

- Lees, J.M., Seismic Tomography in Western Washington, *Ph.D. Dissertation*, University of Washington, 1989.
- Mallick, S., and Frazer, L.N., Practical Aspects of Reflectivity Modeling, *Geophysics*, **52**, 1355-1364, 1987.
- McCullom, R.L., and Crosson, R.S., An Array Study of Upper Mantle Velocity in Washington State, *Bulletin of the Seismological Society of America*, **65**, 467-482, 1975.
- McKee, B., *Cascadia: The Geologic Evolution of the Pacific Northwest*, McGraw-Hill, Inc., New York, 1972.
- Menke, W., *Geophysical Data Analysis: Discrete Inverse Theory*, Academic Press, Inc., Florida, 1984.
- Moran, S.C., Mount St. Helens, 1980-1992: The Dynamics and Evolution of an Active Magmatic System as Inferred from Earthquakes and Focal Mechanisms, *Masters Thesis*, University of Washington, 1992.
- Muller, G., The Reflectivity Method: a Tutorial, *Journal of Geophysics*, **58**, 153-174, 1985.
- Noson, L.L., Qamar, A., and Thorsen, G.W., *Washington State Earthquake Hazards*, Information Circular 85, Washington Division of Geology and Earth Resources, 1988.
- Shirley, K., Columbia Plateau Activity Booms: Magnetotellurics Offers New Looks, *American Association of Petroleum Geologists Explorer*, 1984.
- Turcotte, D.L., and Schubert, G., *Geodynamics: Applications of Continuum Physics to Geological Problems*, John Wiley & Sons, Inc., New York, 1982.
- Walsh, T.J. *et al.*, Geologic Map of Washington -- Southwest Quadrant, Geologic Map

White, D.J., and Clowes, R.M., Shallow Structure Beneath the Juan de Fuca Ridge from 2-D Seismic Refraction Tomography, *Geophysical Journal International*, **100**, 349-367, 1990.

Zelt, C.A., and Smith, R.B., Traveltime Inversion for 2-D Crustal Velocity Structure, *Geophysical Journal International*, **108**, 16-34, 1992.

Zervas, C.E., and Crosson, R.S., Pn Observation and Interpretation in Washington, *Bulletin of the Seismological Society of America*, **76**, 521-546, 1986.

Appendix I

Table A1. Stations used and their geographic locations.

<u>STATION</u>	<u>LATITUDE</u>	<u>LONGITUDE</u>	<u>ELEVATION (km)</u>
HDW	47N38 54.60	123W03 15.20	1.006
GMW	47N32 52.50	122W47 10.80	0.506
SPW	47N33 13.30	122W14 45.10	0.008
MEW	47N12 07.00	122W38 45.00	0.0975
GHW	47N02 30.00	122W16 21.00	0.268
RMW	47N27 34.95	121W48 19.20	1.024
GSM	47N12 11.40	121W47 40.20	1.305
RVC	46N56 34.50	121W58 17.30	1.000
FMW	46N56 29.60	121W40 11.30	1.859
RER	46N49 09.20	121W50 27.30	1.756
WPW	46N41 53.40	121W32 48.00	1.250
GLK	46N33 50.20	121W36 30.70	1.320
TWW	47N08 17.20	120W52 04.50	1.046
ELL	46N54 34.80	120W33 58.80	0.789
YAK	46N31 43.80	120W31 14.40	0.629
MOX	46N34 38.00	120W17 35.00	0.540
VTG	46N57 28.80	119W59 14.40	0.208
BVW	46N48 30.60	119W52 48.00	0.707
BRV	46N29 07.20	119W59 29.40	0.925
MDW	46N36 48.00	119W45 39.00	0.330
WA2	46N45 24.20	119W33 45.50	0.230
GBL	46N35 51.60	119W27 35.40	0.330
RSW	46N23 28.20	119W35 19.20	1.037
PRO	46N12 45.60	119W41 09.00	0.552
WIW	46N25 48.80	119W17 13.40	0.130

Appendix II

Table A2. Earthquakes used, their locations and x-distances.

<u>Event # and Tag</u>	<u>LAT</u>	<u>LONG</u>	<u>DEPTH (km)</u>	<u>X-DIST (km)</u>
Event #1 91072501463	47N2779	122W3664	25.0	0.0
Event #2 92080608001	46N0147	118W1598	12.0	368.0
Event #3 92010611034	46N4995	120W4130	11.0	162.0
Event #4 92070720595	47N0731	121W1636	3.0	109.0
Event #5 92051716211	46N2723	119W3679	14.0	254.0
Event #6 91111423011	47N2358	122W1635	10.0	26.2
Event #7 92082402023	46N2050	119W1451	10.0	286.0
Event #8 90042010162	46N4634	120W0401	1.0	208.0
Event #9 90031708392	47N1962	122W1762	5.0	27.9
Event#10 92071420014	45N5860	118W1610	12.0	370.7
Event#11 91031620165	47N1421	122W4036	52.0	1.5
Event#12 90121016191	46N3774	120W4233	10.0	172.8
Event#13 91010417460	47N0514	121W4493	17.0	81.6
Event#14 91032219434	47N0478	121W2104	2.0	104.5
Event#15 91040417144	46N0491	118W5001	8.0	326.7
Event#16 91060421421	46N0453	118W4509	12.5	332.6
Event#17 91071401180	47N1381	121W5458	18.0	58.9
Event#18 92022104373	46N4433	120W5701	4.0	150.5
Event#19 92073005101	46N3573	120W2961	2.0	187.8
Event#20 88031110012	47N1125	122W1517	62.0	33.3
Event#21 93012617053	47N2231	122W4135	24.0	-2.1
Event#22 88102908465	47N3946	122W5171	55.0	-27.0
Event#23 87042806423	47N3675	122W4652	25.0	-18.8
Event#24 89062102335	47N3953	122W5910	53.0	-35.0
Event#25 92031820434	47N3991	123W1075	13.0	-48.3

Appendix III

Table A3. Actual station movement. "Mean" represents the station's average x-distance, and "deviation" represents the movement about that mean.

<u>STATION</u>	<u>MEAN (km)</u>	<u>DEVIATION (+/- km)</u>
HDW	-37.2	2.0
GMW	-15.5	3.3
SPW	21.2	0.55
MEW	26.2	0.0
GHW	44.75	10.45
RMW	55.75	15.85
GSM	68.2	0.1
RVC	66.75	14.45
FMW	85.8	13.0
RER	76.0	21.8
WPW	115.3	12.0
GLK	120.5	20.1
TWW	128.3	13.4
NAC	155.5	8.6
ELL	162.8	10.4
YAK	191.0	7.0
MOX	193.25	13.0
VTG	214.9	23.8
BVW	224.3	14.8
BRV	231.5	8.9
MDW	239.1	6.1
WA2	240.75	20.65
GBL	262.8	11.0
RSW	259.5	4.5

Appendix IV

Table A4. 1-Dimensional starting models.

Eastern Washington from Glover (1985)

Depth (km)	Velocity(km/sec)
0.0	3.70
0.4	5.15
8.5	6.10
13.0	6.40
23.0	7.10
38.0	7.90

Puget Sound from Crosson (1976)

Depth (km)	Velocity(km/sec)
0.0	5.40
4.0	6.38
9.0	6.59
16.0	6.73
20.0	6.86
25.0	6.95
41.0	7.80

Appendix V

Table A5. Resolution and standard errors for final model velocity nodes. Nodes are numbered with their layer numbers and then left to right starting with number 1. The letters designate (u) upper layer velocities and (l) lower layer velocities. For example, 2l6 means 2nd layer, lower layer, 6th node. The uncertainty for all nodes was $\sigma = 0.20$ km/sec.

<u>NODE</u>	<u>RESOLUTION</u>	<u>STANDARD ERROR (km/sec)</u>
2u1	0.0224	0.1977
2u6	0.1829	0.1808
2u7	0.0958	0.1902
2u8	0.1628	0.1830
2u9	0.1926	0.1797
2u10	0.2380	0.1746
2u11	0.3655	0.1593
2u12	0.2848	0.1691
2u13	0.0371	0.1963
2u14	0.0000	0.2000
2l1	0.0090	0.1991
2l6	0.2048	0.1784
2l7	0.1841	0.1807
2l8	0.2675	0.1712
2l9	0.3013	0.1672
2l10	0.3533	0.1608
2l11	0.3104	0.1661
2l12	0.0970	0.1901
2l13	0.0005	0.1999
3u1	0.0455	0.1954
3u2	0.3689	0.1589

311	0.0668	0.1932
312	0.3534	0.1608
315	0.0864	0.1912
316	0.3357	0.1630
317	0.1979	0.1791
319	0.2368	0.1747
3110	0.0157	0.1984
4u1	0.0006	0.1999
4u2	0.0523	0.1947
4u4	0.2186	0.1768
4u6	0.3401	0.1625
4u7	0.6402	0.1200
4u8	0.6363	0.1206
4u10	0.3656	0.1593
411	0.0002	0.2000
414	0.0658	0.1933
415	0.1744	0.1817
417	0.5916	0.1278
419	0.5355	0.1363
4110	0.1311	0.1864
5u1	0.0143	0.1986
5u2	0.8293	0.0826
5u3	0.9276	0.0538
5u4	0.5975	0.1269
511	0.0037	0.1996
512	0.5876	0.1284
513	0.7950	0.0906

